

The Cyclogenesis Butterfly: Uncertainty growth and forecast reliability during extratropical cyclogenesis

Mark J. Rodwell¹ and Heini Wernli²

¹European Centre for Medium-Range Weather Forecasts, Reading, UK

²Institute for Atmospheric and Climate Science, ETH Zürich, Switzerland

Correspondence: Mark Rodwell (mark.rodwell@ecmwf.int)

Abstract.

~~Global numerical weather prediction is often limited by Lorenz-type “butterflies” in the flow. Here we think of these as local flow configurations associated with pronounced uncertainty growth rates, as demonstrated in short-range ensemble predictions. Some of these configurations correspond to potential instabilities of~~ The chaotic and multi-scale nature of the atmosphere was brought into the public imagination by the question of Lorenz in 1972: “Does the flap of a butterfly’s wings in Brazil set off a tornado in Texas?”. While numerical models currently used in global weather prediction have grids which certainly do not resolve butterflies, they nevertheless display strong sensitivity to initial conditions. In ensemble forecasts, this sensitivity is manifested in the growth of ensemble variance with leadtime. Interestingly, in the extratropics, this uncertainty growth appears to be organised in particular synoptic flow configurations which, for the purposes of practical prediction,

5 might be thought of as large, metaphorical ‘butterflies’ in the flow. Often, forecasts for severe downstream weather ~~only show an show marked~~ improvement in skill when these ~~butterflies-‘butterflies’~~ have passed. Here we focus on the “eyelogenesis butterflyCyclogenesis Butterfly” — associated with baroclinic and convective instabilities in the extratropics. One question addressed is how do different We investigate four ~~operational ensemble forecast systems (within the “TIGGE” archive) represent the associated uncertainty growth rates? To test which might be “better”, within the TIGGE archive, and find that~~

10 they display quite different initial uncertainty growth rates in cases of cyclogenesis. Evaluation through use of an extended spread-error equation ~~is used to investigate how well these non-linear models maintain short-range statistical reliability during eyelogenesis.~~ shows that some models fail to maintain short-range statistical reliability within the North Atlantic stormtrack during winter 2020/21. For the European Centre for ~~Medium-Range Medium-Range~~ Weather Forecasts (ECMWF) ensemble, considerable short-range over-spread is found in the North Atlantic stormtrack during winter 2020/21 — representing a source

20 of untapped predictability (this result appears to generalise to other stormtracks and at least one other model). Flow-type flow-type ~~clustering demonstrates that this over-spread is directly associated with the representation of cyclogenesis. We attempt to quantify the contributions to the~~ its ‘over-spread’ in the stormtrack is indeed associated with cyclogenesis events. At day 2, a large part of the ~~total spread in cyclogenesis cases~~ from is associated with the growth of ~~initial uncertainty (as derived from ensemble data assimilation), singular vector perturbations, and model uncertainty. At day 2, we find that~~ but ~~up to 25%~~

25 can be associated with the ~~singular vectors~~ additional singular vector perturbations to the initial conditions, and up to 25% with the representation of ~~model uncertainty. The over-spread suggests that reductions in forecast error over recent years would~~

~~permit further development of these uncertainty aspects. The sensitivities of spread to resolution, the explicit representation of convection, and the assimilation of local observations provide additional insight for future development are also considered. The study raises the question whether a reduction in singular vector perturbations, to improve stormtrack reliability, would then allow short-range diagnostics to better inform further model and model-uncertainty development, which could be beneficial throughout the forecast range.~~

1 Introduction

~~In The chaotic nature of the atmosphere, with its large sensitivity to small perturbations (Sutton, 1954; Lorenz, 1963, 1972), poses a challenge for numerical weather prediction (NWP), ensembles comprising multiple forecasts are generally made (Lewis, 2005) to represent the chaotic growth of initial and model uncertainty (Sutton, 1954; Lorenz, 1963). The aim of these ensembles is to estimate the solution to the Liouville equation (Ehrendorfer, 1994), which describes the state-vector distribution of an infinite set of trajectories, as they diverge from their initial conditions on the system's attractor. The initial distribution for ensemble forecasts is generally obtained through data assimilation (Rabier et al., 2000; Humpherys et al., 2012), in particular ensemble data assimilation (Isaksen et al., 2010) which aims to represent flow-dependent error covariances in the background or "first-guess" (Bonavita et al., 2016) and in the observations (Geer et al., 2018), as well as model uncertainty (MU; Buizza et al., 1999) and a model grid's lack of representativity of point observations (Janjić et al., 2018). In some cases (including at ECMWF) "singular vector" (SV; Molteni and Palmer, 1993) perturbations, which represent the most strongly growing modes over a finite time interval (in . To embrace this challenge, NWP has developed ensemble techniques, whereby a set (or ensemble) of initial conditions, representing the uncertainty in the current state, is used to initialise an ensemble of forecasts (Palmer et al., 1992; Molteni et al., 1996). The variance of the linear regime), are applied to the distribution of initial conditions as a pragmatic means of boosting ensemble divergence. ensemble, which generally grows with leadtime, is then a measure of forecast uncertainty — something of great interest to the user.~~

~~As implied by the existence of SVs, the divergence of trajectories within state-space is not uniform over the attractor, and weather predictability is often limited by the Lorenz-type "butterflies" in the flow (Lorenz, 1972). Here we think of these as local flow configurations where the chaotic and exponential growth-rate of uncertainty is particularly strong. Some of these configurations correspond to potential instabilities of the flow — baroclinic (Lillo and Parsons, 2017) and convective (Sun and Zhang, 2016; Rodwell et al., 2018) for example. The This study focuses on uncertainty growth in the North American / North Atlantic / European region, and particularly the North Atlantic winter stormtrack, with its embedded cyclogenesis events and other synoptic systems. Synoptic scales are particularly important in NWP because these become the largest contributor to global ensemble variance over the first few days of the forecast (Tribbia and Baumhefner, 2004). Previous studies have shown that occasional drops in weather forecast performance in the region of interest can be related to particular prior synoptic flow situations. These include baroclinic flows propone to cyclogenesis (Lillo and Parsons, 2017), situations of convective instability (Rodwell et al., 2013; Sun and Zhang, 2016), the extratropical transition of tropical cyclones (TCs) can lead to a strong growth of uncertainty (Riemer and Jones, 2014) with implications for severe weather downstream (Grams and Blumer, 2015). This is~~

60 perhaps an example of a more general issue associated with the interaction of a cut-off vortex with an upper-tropospheric trough (Grams et al., 2018; Baumgart and Riemer, 2019). Sometimes the seeding of uncertainty growth can be traced further back in time by regressing the ensemble against itself at an earlier lead time. For example, strong growth of uncertainty in the ECMWF ensemble during the interaction of TC Humberto with an extratropical upper-tropospheric trough in 2019 appeared to be seeded with local uncertainties in the TC three days earlier (not shown). Strong uncertainty growth for Mediane
65 Zorbas in 2018, associated with large uncertainties in the position of a potential vorticity streamer over the Mediterranean, has also been linked to the downstream propagation of uncertainties in the North Atlantic waveguide several days before (Portmann et al., 2020).

(Riemer and Jones, 2014), development of cut-off vortices, and their interaction with upper-tropospheric troughs (Grams et al., 2018; Baumgart and Riemer, 2019). The impacts of these events on jet stream/waveguide dynamics can lead to errors and uncertainties in downstream ‘blocking’ (Rodwell et al., 2013) and extreme precipitation (Grams and Blumer, 2015). A ‘Lagrangian growth rate’ diagnostic (Rodwell et al., 2018) highlights these flow configurations as situations of enhanced 12 h growth in synoptic-scale ensemble spread in upper-tropospheric potential vorticity. The possibility that this growth rate diagnostic provides a useful means of systematically studying the flow-dependence of forecast skill and reliability motivates the present study. Here, the focus is on the strong growth rates associated with extratropical cyclogenesis — hence the term ‘The Cyclogenesis Butterfly’. It should be emphasised that this
70 term refers to the sensitivity to initial uncertainty derived from operational ensemble data assimilation (Isaksen et al., 2010), rather than intrinsic growth rates associated with the atmosphere’s sensitivity to small scale perturbations (Lorenz, 1963, 1972). See, e.g., Durran and Gingrich (2014) and Palmer et al. (2014) for interesting discussions. Although the location and structure of the early uncertainty growth will reflect the SVs of the flow (even when SV perturbations have not been explicitly applied), the magnitude of the growth rate will depend on how strongly the uncertainty projects onto these SVs (Leutbecher and Lang, 2014). Beyond
80 the linear regime, growth rates might be different again. Operational ensembles may differ from the true growth rate due to necessary approximations, although the stochastic representation of model uncertainty (Buizza et al., 1999) underlying processes driving growth (Baumgart et al., 2019) are likely to be similar, global operational ensembles generally require a representation of ‘model uncertainty’ (MU; Buizza et al., 1999) — which aims to account for these approximations (Christensen, 2020). Hence there is a need to evaluate the state-dependent growth rate of uncertainty within operational forecasts. Here the focus
85 is on what is termed here the “cyclogenesis butterfly” missing interactions with scales that are unresolved on the model grid — associated with the intensification of extratropical cyclones. The key question in order to achieve forecast ‘reliability’ (Gneiting and Raftery, 2007; Rodwell et al., 2020).

While there are clear differences with intrinsic growth rates (Selz et al., 2022), a useful comparison might be made between different operational ensemble systems — for example those available in near real-time from ‘The International Grand Global
90 Ensemble’ (TIGGE, Swinbank et al., 2016) archive. A question addressed here is “How well do models maintain statistical reliability during composites of cyclogenesis events?” The metric of reliability, discussed more fully in section ??, being an extension of the “similar are the growth rates in such ensembles in cases of extratropical cyclogenesis?” A means of evaluating each system’s short-range ‘reliability’ (Gneiting and Raftery, 2007; Rodwell et al., 2020) would be useful in this comparison. At short-ranges, the ‘spread-error’ relationship: which states that the mean ensemble variance (Spread^2) should agree with

95 the mean-squared error of the ensemble-mean (Error^2). In line with the examples discussed above, much of the focus of this study is on reliability in the upper-troposphere, where uncertainties can propagate along the Jetstream / wave-guide and give rise to uncertainties in down-stream features such as anticyclonic “blocking” and extreme precipitation’ reliability equation (Leutbecher and Palmer, 2008, which states that the mean ensemble variance should agree with the mean-squared-error of the ensemble m
to be extended to account for biases and non-negligible uncertainties in the verifying analysis. When combined with flow-type
100 clustering, the approach should allow a flow-dependent evaluation of short-range reliability and initial growth rates — something this study attempts to do. These could depend on, for example, the reliability of initial conditions (Rodwell et al., 2016), whether an ensemble system employs singular vector (SV; Molteni and Palmer, 1993) perturbations to boost initial growth rates, how convection is parametrized or resolved (Wedi et al., 2020) and, as discussed above, how MU is represented. In the absence of SV perturbations, the potential is raised that developments to the model and MU, which improve flow-dependent
105 short-range reliability, will be beneficial throughout the forecast range.

The study is structured as follows. Section 2 gives details of the data used. This includes data obtained for several of the world’s operational ensemble forecasting systems from the “TIGGE” archive. Section 3.1 introduces two cyclogenesis case studies, and Section ?? lists the data sources used. (There is a series of methodologies employed in the study — these are discussed later, once the motivation for their use becomes apparent). Section 3 discusses the quantification of uncertainty
110 growth rates. Section ?? then calculates these growth rates for the two case studies, and highlights differences between operational forecast systems in the TIGGE archive. To assess how well statistical reliability is maintained during such events, an “extended spread error equation” is derived in Section ?. This accounts for bias and analysis uncertainty to permit the assessment of reliability at all lead times. In Section 4.1 the extended spread error equation is applied to two TIGGE models for the December 2020 – February 2021 (DJF 2020/21) season at a lead time of two days. To differing extents, both models
115 are shown to be “over-spread” in the region of the North Atlantic stormtrack. Focusing on the western part of the North Atlantic stormtrack, a clustering technique is used in Section 4.1 to identify cyclogenesis events in DJF 2020/21. Section 4.1 demonstrates that the seasonal-mean over-spread is associated mainly with these cyclogenesis events. Section 5 returns to the case studies from Section 3.1 to quantify the spread contributions from initial and model uncertainty, and to explore the sensitivity to resolution, the explicit representation of convection, and the assimilation of local observations, and interpretation
120 of uncertainty growth rates, with particular application to cyclogenesis. Section 4 discusses forecast reliability in the presence of bias and uncertainty in the verifying analyses, with application to seasonal means in the North Atlantic stormtrack region, and when composited on cyclogenesis cases. Section 5 investigates the sources of uncertainty in cyclogenesis cases. Conclusions and a discussion are presented in Section 6. The Appendix is used to provide some mathematical derivations, further detail, and additional figures. Supplementary material includes animations of uncertainty growth rates, a discussion about
125 prospective research are given in Sect. 6. Supplementary material includes animations of uncertainty growth rates.

2 Data

2 Models, data sources and key parameters

Here, a brief description of the datasets used is given. Further details are provided later in the text. The ECMWF re-analysis version 5 (ERA5; Hersbach et al., 2020) is used to show the analysed development of the two case studies. The background forecasts from the

2.1 The ECMWF ensemble assimilation and forecast system

The underlying earth system model for the ECMWF Ensemble of Data Assimilations (EDA; Isaksen et al., 2010) are used to diagnose flow-dependent growth rates in the standard deviation of (isentropic) potential vorticity (PV) for the ECMWF model. Further information on the Data Assimilations (EDA; Isaksen et al., 2010), and Ensemble forecast (ENS; Palmer et al., 1992; Molteni et al., 2015) spherical harmonics to compute much of the dynamics, with physical parametrizations computed in grid-point space. Of particular interest here is the parametrization of convection, which was originally based on Tiedtke (1989), but includes revisions to entrainment and coupling with the large scale (Bechtold et al., 2008; Hirons et al., 2013), and improvements in the diurnal cycle of convection through use of a modified convective available potential energy (CAPE) closure (Bechtold et al., 2014).

The 50-member EDA used here has a nominal horizontal grid resolution of ~ 16 km. More specifically, in the final EDA iteration, the underlying non-linear model retains a “Triangular” configuration of spherical harmonics with total wavenumbers ≤ 639 and uses a “Cubic octahedral” grid so that 4 grid points represent the smallest waves (the resolution is thus summarised as TCo639), has 137 levels in the vertical (L137) and uses a 12 min timestep. 4D Variational data assimilation (4DVar, Rabier et al., 2000) uses the full non-linear model, together with ‘tangent-linear’ and adjoint versions, to extract the information content from many millions of conventional and satellite observations during each 12 h analysis cycle. This is done by first screening observations and correcting them using Variational Bias Correction (VarBC, Dee, 2004). For each EDA member, the observations are then randomly perturbed to simulate observation uncertainty (Isaksen et al., 2010). The ‘background’ for a given EDA member is the non-linear forecast initialised from the same member’s previous analysis. The estimated uncertainty in this forecast is based on the variances and correlations between the ensemble of background forecasts, with a climatological contribution to correlations for improved stability. For each EDA member, 4DVar combines its background forecast and perturbed observation set in a way that is consistent with the estimated uncertainties in the background (Bonavita et al., 2016) and observations (Geer et al., 2018). An additional unperturbed EDA member, with no perturbations to the observations, is also made.

The EDA is presented in Appendix ???. The International Grand Global Ensemble (TIGGE-) archive (Swinbank et al., 2016) used to initiate a 50-member ENS, with resolution TCo639, L91 and a 12 min timestep. Initial conditions are re-centred on a more recent (“Early Delivery”) unperturbed high-resolution (HRES) 4DVar analysis. ‘Singular Vector’ (SV; Molteni and Palmer, 1993; Leutbecher et al., 2007) are added to the initial conditions as a pragmatic means of boosting ENS spread over the first 2 days. A model uncertainty (MU) parametrization, which partly aims to represent scale interactions with (missing) sub-grid-scale variations, is important for the general growth of ENS spread into the medium-range (e.g., to day 10). Here, this MU representation is based on

160 “Stochastic Perturbation to Physical Tendencies” (SPPT, Buizza et al., 1999), which represents a perturbation to the *total* physical tendency, and is applied throughout the forecast range. Note that SPPT is also applied to the non-linear model in the perturbed members of the EDA, but there are no SV perturbations in the EDA.

165 The sensitivity experiments discussed in Sect. 5 are based on cycle 46r1 of the ECMWF Integrated Forecasting System (IFS). This cycle was operational from 11 June 2019 to 20 June 2020. In these experiments, VarBC and SPPT are “warm-started” from the operational assimilation, ENS initial condition re-centring is not done, and SV perturbation scaling is based on the current EDA cycle rather than the previous cycle. In the higher-resolution ~ 4 km ENS experiment, the model is run in “single precision” (Váňa et al., 2017; Lang et al., 2021) with resolution TCo2559 L91 and a 4 min timestep.

The study additionally makes use of ECMWF reanalysis version 5 (ERA5; Hersbach et al., 2020), which is also based on the EDA.

2.2 Other ensemble forecast systems in the TIGGE archive

170 In comparisons with ensemble forecasts from other centres, all data are retrieved from the TIGGE archive, which currently contains global ensemble forecasts from about a dozen of the world’s operational forecasting centres (12 centres were present on 1 September 2021). These forecasts are available a few days behind ~~real-time~~ real-time and are a valuable ~~source of data for diagnostic (and other) studies. The four centres focused on here, their archived ensemble sizes (perturbed + control) and data resolutions, are~~ source for diagnostic studies. Three other TIGGE models are compared with the ECMWF model. These are from the Japan Meteorological Agency (JMA, ~~26+1mem, ~ 139 km~~), the United States’ National Centers for Environmental Prediction (NCEP, ~~30+1mem, ~ 56 km~~), and the United Kingdom’s Met Office (UKMO, ~~17+1mem, ~ 32 km~~). The). Salient details of these four ensemble forecast systems are presented in Table 1. For consistency, comparisons are based on 00 and 12 UTC ~~initialisation times are used here for each model, although they are also available at other times for some centres. This data is used to compare flow-dependent growth rates in the standard deviation of geopotential height~~ amongst these four models, and for the systematic extended spread-error evaluation. Finally, a suite of sensitivity experiments is conducted with the ECMWF Integrated Forecast System (IFS) for the two case studies. This includes EDA and ensemble forecast (ENS) aspects. ~~Further information on~~ run times only.

2.3 Potential vorticity

185 A useful quantity for this study is isentropic potential vorticity (IPV, Hoskins et al., 1985), $P = -g(f + \zeta_\theta) \frac{\partial \theta}{\partial p}$. Here, g is the IFS is presented in Appendix ?? gravitational acceleration, f is the Coriolis parameter, p is pressure, θ is potential temperature, and $\zeta_\theta = \mathbf{k} \cdot \nabla_\theta \times \mathbf{v}$ is the isentropic vorticity, where \mathbf{k} is the local unit vertical vector, ∇_θ is the horizontal gradient operator on an isentropic surface, and \mathbf{v} is the horizontal wind vector. IPV is usually measured in PV units (PVU) with $1 \text{ PVU} = 10^{-6} \text{ m}^2 \text{ s}^{-1} \text{ K kg}^{-1}$. A key advantage of using IPV here is that its tendencies due to dynamic and diabatic effects can be readily disentangled:

$$\frac{\partial P}{\partial t} + \mathbf{v} \cdot \nabla_\theta P = \mathcal{D} \quad , \quad (1)$$

Table 1. Details of the four TIGGE models used in this study, valid during the period of investigation. EDA=Ensemble of 4DVar (Isaksen et al., 2010), 4DVar=4D Variational data assimilation (Rabier et al., 2000), EnKF=Ensemble Kalman Filter (Evensen, 1994), ETKF=Ensemble Transform Kalman Filter (Bishop et al., 2001), LETKF=Local Ensemble Transform Kalman Filter (Hunt et al., 2007), SPPT=Stochastic Perturbation to Physical Tendencies (Buizza et al., 1999), SV=Singular Vector (Molteni and Palmer, 1993), RP=Random Parameters (McCabe et al., 2016), SKEB=Stochastic Kinetic Energy Backscatter (Shutts, 2004).

Centre	ECMWF	JMA	NCEP	UKMO
Resolution (nominal)	16 km	42 km	25 km	21 km
Vertical levels	91	100	64	70
Number of perturbed members	50	26	30	17
Run times (UTC)	0,12	00,12	00,06,12,18	00,06,12,18
Initial perturbation strategy	EDA, SV	LETKF, SV	EnKF	ETKF
Model uncertainty representation	SPPT	SPPT	SPPT, SKEB	RP, SKEB

190 where \mathcal{D} represents the effects of non-conservative (diabatic and frictional) processes (Holton, 2004, Eq. 4.36). IPV is thus conserved following the horizontal flow on an isentrope in the absence of such processes. This study will use P_{315} , the IPV on the 315 K isentrope, which typically intersects the dynamical tropopause ($P=2$ PVU) during winter in the midlatitudes.

3 Introducing two case studies of Cyclogenesis and the cyclogenesis butterfly growth of uncertainty

3.1 An example of cyclogenesis

195 Before performing a more systematic investigation of the “cyclogenesis butterfly”, two cases are selected to ‘cyclogenesis butterfly’, a specific case of North Atlantic cyclogenesis is selected to illustrate and highlight the salient features in its development and its uncertainty. The cases were chosen because they were case was chosen because it was quite “clean”, without being strongly affected by other flow perturbations in their environment, and because they involved both baroclinic and diabatic aspects. However, the speed of cyclogenesis and growth of uncertainty were not considered in the choice. Figure 1 introduces

200 the main synoptic-scale flow features of the two event. The cyclone of Case 1 develops on 26 November 2019 over the U.S. eastern North America (not shown). By 18 UTC on 27 November a day later, it reaches the Great Lakes with a minimum sea level pressure (SLP) pressure at mean sea level (PMSL) of about 990 hPa. The cyclone then (not shown). At 18 UTC on 28 November, the cyclone reaches the North American east coast with a similar intensity (Fig. 1a). There is a cutoff in PV on the 315 potential vorticity on the $\theta = 315$ K isentrope (PV_{315}) aloft, and intense surface rainfall

205 in the region identified as a warm conveyor belt (WCB). One day later (Fig. 1b), the cyclone has strongly deepened to below 974 hPa as it moves slowly out into the Atlantic. Intense precipitation continues in the WCB ascent regions along the cold and bent-back fronts. The cyclone of Case 2 first occurs as a weak system with a SLP minimum larger than 1010 bent-back fronts. In the next 24 hPa over Ohio at 00h, the cyclone remains stationary, and it deepens further to below 970 UTC on 16 January 2020 (not shown). It then propagates to the North Atlantic and deepens to less than 990 hPa ahead of a broad trough over eastern

210 North America at 00 UTC on 17 January, again with strong precipitation along the WCB ascent (Fig. 1c). During the next day, the cyclone deepens explosively and reaches a core pressure of ~ 960 hPa as it travels over the Atlantic south of Newfoundland (Fig. 1d). At that time the WCB extends from 25 to 55°N to 50°N, associated with intense precipitation, and the $PV_{315} = 2$ PVU contour shows a prominent trough-ridge pattern over the western and central North Atlantic, and the P_{315} pattern attains the classical structure of a mature cyclone, with a large-amplitude trough-ridge dipole up- and downstream of the surface cyclone, respectively. The heterogeneity of the precipitation rate along the WCB is reminiscent of the occurrence of embedded convection (Oertel et al., 2020). This brief overview emphasizes the strong deepening of the ~~two systems~~ system off the North American east coast and ~~their~~ ~~its~~ combined baroclinic and diabatic character. Forecast experiments that investigate the strong ~~cyclone deepening period for this case~~ are initialised at 12 UTC on 28 November 2019, and therefore the dates shown in Fig. 1 correspond to forecast days 0, 1 and 00 UTC on 17 January 2020, 2.

4 The uncertainty growth rate

3.1 The Lagrangian growth rate

The local uncertainty growth rate of an ensemble forecast can be quantified as $\hat{\sigma}^{-1} \partial \hat{\sigma} / \partial t$ where $\hat{\sigma}$ is estimated as $\hat{\sigma}_x^{-1} \partial \hat{\sigma}_x / \partial t$ where $\hat{\sigma}_x$ is the ensemble standard deviation of some 1-dimensional state measure (of the atmosphere). Since much of this local growth rate atmospheric parameter field X (the circumflex $\hat{\cdot}$ indicates a sample estimate throughout this study) and t is the forecast leadtime. As observed by Rodwell et al. (2018), a large component of the local growth rate can be associated with the advection of uncertainty, Rodwell et al. (2018) calculated a “Lagrangian” growth rate $\hat{\sigma}^{-1} (\partial \hat{\sigma} / \partial t + \bar{v} \cdot \nabla \hat{\sigma})$, which follows the ensemble-mean horizontal flow \bar{v} . The state measure used by Rodwell et al. (2018) was isentropic potential vorticity and it is useful to separate this off to highlight the processes driving uncertainty growth. If X is chosen to be IPV P on some upper tropospheric isentrope θ . Following the derivation of Baumgart and Riemer (2019), but with a different formulation, the growth rate of this measure can be related to sources of uncertainty growth via the equation, then Eq. (1) provides a straightforward approach to achieve this. Firstly, it is useful to establish some notation. For any parameter Y (e.g., P , v , D), write Y_i for its value in ensemble forecast member $i \in \{1, \dots, m\}$. Using an overline to denote a mean $\bar{Y} = m^{-1} \sum_i Y_i$ (even for non-linear terms: $\bar{YZ} = m^{-1} \sum_i Y_i Z_i$) and a prime to denote deviations from the mean $Y'_i = Y_i - \bar{Y}$, then the

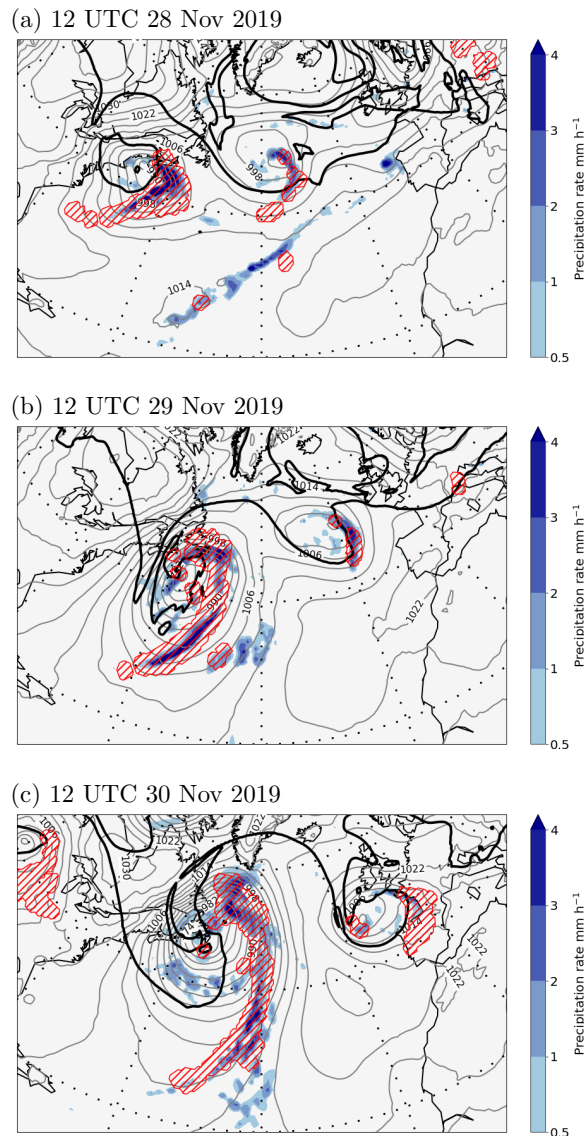


Figure 1. Synoptic overview, based on ERA5 reanalyses, of [the two a North Atlantic cyclogenesis events event](#) at [\(a,b\) 12 UTC on \(a\) 28 and November, \(b\) 29 November 2019 for Case 1](#), and [\(c,d\) 00 UTC on 17 and 18 January 2020 for Case 2](#). [30 November 2019](#). Shown are [SLP-PMSL](#) (grey contours at intervals of 4 hPa), surface precipitation accumulated over the previous hour (colour shading, in mm h^{-1}), the [PV315 = 2 PVU](#) contour indicating the tropopause on 315 K (black solid line), and the WCB ascent region (red hatching). WCBs are identified as 48 h trajectories that ascend from the lower troposphere by more than 600 hPa [in 48 h](#) (e.g., Wernli and Davies, 1997; Madonna et al., 2014), and the ascent region (shown [in with red hatching](#)) corresponds to the envelope of the horizontal positions of all WCB trajectories, [initialized every 6 h](#), that are located between 800 and 500 hPa at the indicated time [\(corresponding approximately to their mid-ascent time\)](#).

235 variance estimator for P can be written as $\widehat{\sigma}_P^2 = \overline{P'^2}$. Using this notation and the results that $\overline{Y'} = 0$ and $\overline{Y'Z} = 0$, the local growth rate for P can be written as

$$\begin{aligned}
 \frac{1}{\widehat{\sigma}_P} \frac{\partial \widehat{\sigma}_P}{\partial t} &= \frac{1}{2\widehat{\sigma}_P^2} \frac{\partial \widehat{\sigma}_P^2}{\partial t} \\
 &= \frac{1}{2\widehat{\sigma}_P^2} \frac{\partial \overline{P'^2}}{\partial t} \\
 &= \frac{1}{\widehat{\sigma}_P^2} \overline{P' \left(\frac{\partial P}{\partial t} - \frac{\partial \overline{P}}{\partial t} \right)} \\
 &= \frac{1}{\widehat{\sigma}_P^2} \overline{P' (\mathcal{D} - \mathbf{v} \cdot \nabla_\theta P)} \\
 &= \frac{1}{\widehat{\sigma}_P^2} \overline{P' (\mathcal{D}' - \overline{\mathbf{v}} \cdot \nabla_\theta P' - \mathbf{v}' \cdot \nabla_\theta P)} \\
 &= -\frac{1}{2\widehat{\sigma}_P^2} \overline{\mathbf{v} \cdot \nabla_\theta P'^2} + \frac{1}{\widehat{\sigma}_P^2} \overline{P' (\mathcal{D}' - \mathbf{v}' \cdot \nabla_\theta P)} \\
 &= -\frac{1}{\widehat{\sigma}_P} \overline{\mathbf{v} \cdot \nabla_\theta \widehat{\sigma}_P} + \frac{1}{\widehat{\sigma}_P^2} \overline{P' \mathcal{D}'} - \frac{1}{\widehat{\sigma}_P^2} \overline{P' \mathbf{v}' \cdot \nabla_\theta P} \quad ,
 \end{aligned} \tag{2}$$

Here, an overline denotes a mean over ensemble members, and a prime denotes an ensemble member's deviation from the mean. The “standard” (biased) estimator for variance is used throughout this study (with the bias explicitly removed where necessary) so that here $\widehat{\sigma}^2 = \overline{P'^2}$. The NC are the “non-conservative” tendencies in potential vorticity associated with diabatic and frictional processes for each ensemble member (see Appendix ?? for the derivation). Following the discussion of Baumgart and Riemer (2019), when Eq. (??) is applied to the upper troposphere, it shows how the growth rate for PV will reflect local non-conservative processes including near-tropopause radiative forcing (Chagnon et al., 2013). This is a different formulation of the equation explored by Baumgart and Riemer (2019); their equation (8). The first term on the last line is the advection of uncertainty by the ensemble mean wind. Rearranging, we can define a ‘Lagrangian growth rate’ for IPV as

240

245

$$\text{LGR}_P \equiv \frac{1}{\widehat{\sigma}_P} \left\{ \frac{\partial \widehat{\sigma}_P}{\partial t} + \overline{\mathbf{v}} \cdot \nabla_\theta \widehat{\sigma}_P \right\} = \frac{1}{\widehat{\sigma}_P^2} \overline{P' \mathcal{D}'} - \frac{1}{\widehat{\sigma}_P^2} \overline{P' \mathbf{v}' \cdot \nabla_\theta P} \quad . \tag{3}$$

The left side of Eq. (3), as in Rodwell et al. (2018), represents the rate of growth of the ensemble standard deviation of P following the ensemble mean horizontal flow on an isentrope. The two terms on the right hand side of Eq. (3) provide a useful glimpse at the interactions that drive this growth. The second term on the right is the covariance between P' and the advection of PV by each member's anomalous wind $\mathbf{v}' \cdot \nabla_\theta P$. This term represents the effect of interactions between dynamical uncertainties at all (resolved) scales. In the case of initial growth rates in operational ensemble forecasts, this could include interactions with large-scale analysis uncertainties, particularly positive contributions associated with cyclogenesis (*viz* Hoskins et al., 1985, their Fig. 21) since there is as much variance power in the EDA at scales ~ 5000 km as there is at

250

scales ~ 50 km. (Maximum EDA variance contributions come from intermediate scales ~ 400 km — illustrative power spectra are presented in Fig. B1 in Appendix B). This initial large-scale contribution is likely to be in contrast to some predictability studies (Judt, 2018), which apply grid-point Gaussian noise and where the smallest resolved scales will dominate the total initial variance. In addition, if (dry) singular vector perturbations are applied to the initial conditions for the operational forecast (Table 1), then the growth associated with baroclinic uncertainties will be accentuated. The first term on the right hand side of Eq. (3) represents covariances between P' and non-linear advective tendencies due to e. g. upper tropospheric Rossby-wave dynamics (emphasized by Baumgart and Riemer, 2019), deep tropospheric interaction associated with baroclinic instability (e.g. Hoskins et al., 1985), and upper tropospheric divergence associated with dry balanced dynamics (as represented by the “Omega equation” mid-tropospheric diabatic forcing (e.g. Rodwell et al., 2013). non-conservative processes D' . There is the possibility for negative growth rate contributions here, associated with the effects of latent heating on upper tropospheric D' during cyclogenesis (viz Ahmadi-Givi et al., 2004, their Fig. 14). Here too, there could be differences with intrinsic growth rates — for example, due to the need to parametrize turbulent processes, and because the model uncertainty representation can only approximate the effects of interactions with sub-grid-scale variations. In operational and intrinsic contexts, as the leadtime increases and smaller scale uncertainties become saturated, the larger scales will become increasingly important for driving further growth. Hence there is no fixed ‘ground-truth’ with which to evaluate modelled growth rates. Nevertheless, it is informative to calculate operational growth rates, and to compare these for different models.

Note that there is a natural link between the growth rate and In Sect. 3.2, the growth rate on the left side of Eq. (3) will be calculated from the background forecasts of the rate of change of the density of state trajectories in the Liouville Equation (as discussed in section 1). Focusing on the probability density function (pdf) of any 1-dimensional state measure, for small (initial) uncertainty and assuming the shape of the pdf does not change greatly over a short (~ 12 EDA. The right side of Eq. (3) is discussed further in relation to prospective research in Sect. 6.

3.2 Uncertainty growth in the EDA

This study is interested in the growth of synoptic scale uncertainty (due to interactions between all scales) during the first few days of the ensemble forecast. To focus on this growth, LGR_r is filtered with a synoptic spatio-temporal filter. This multiplies spectral coefficients with total wavenumber $n > n_s = 21$ by $\{n_s(n_s + 1)\}/\{n(n + 1)\}$ so that scales larger than ~ 700 h forecast (only its mean and variance change), then $\hat{\rho} \propto \hat{\sigma}^{-1}$ where $\hat{\rho}$ is an estimate of the relative likelihood of the ensemble mean (the value of the pdf at the ensemble mean). Hence, for example, its rate of change following the ensemble mean horizontal flow can be estimated as minus the growth rate, $\hat{\rho}^{-1}(\partial\hat{\rho}/\partial t + \mathbf{v} \cdot \nabla\hat{\rho}) = -\hat{\sigma}^{-1}(\partial\hat{\sigma}/\partial t + \mathbf{v} \cdot \nabla\hat{\sigma})$ km are retained. The filter also includes a 24 h running-mean. To understand how growth rates depend on the synoptic flow situation, it is useful to consider very short leadtimes when all ensemble members are representing essentially the same synoptic flow situation. A natural choice is to use the short background forecasts from ensemble data assimilation.

Figure 2 and Fig. ?? show a single frame from animations of the two cyclogenesis events, shows (shaded) the filtered LGR_p for P_{315} based on the EDA 12 h background forecasts, centred at 12 UTC on 29 November 2019 (one day into the strong cyclogenesis period). Shading depicts the P_{315} uncertainty growth-rate following the ensemble-mean flow, the red contour shows where $P_{315} = 2$ shown in Fig. 1). The caption to Fig. 2 provides technical details of the calculation of LGR_p . Also shown in Fig. 2, from the unperturbed EDA member, are $P_{315} = 2$ PVU (red contour) and vectors display the 850 hPa horizontal wind field (v_{850} , coloured blue when the 850 hPa horizontal moisture flux exceeds $100 \text{ g kg}^{-1} \text{ m s}^{-1}$), both from the control (unperturbed) forecast. Black dots indicate the ensemble-mean precipitation rate. The animations are based on the ensemble of 12 h background forecasts made within the EDA for a sequence of analysis cycles. By concatenating these cycles and applying a “synoptic” spatio-temporal smoothing, the animations follow closely the true evolution of Large LGR_p values are seen at the southern extent of the synoptic flow, and highlight the features associated with enhanced growth-rates. Further details are in the caption to upper-level trough. Note that the orange contours at the centre of this region have the same interval as that of the shading, and indicate values in excess of 0.18 h^{-1} . This location of large LGR_p values appears consistent with Hoskins et al. (1985), discussed above, but further investigation would be useful. Also evident in Fig. 2 and in the Appendix Section ?? The animations of the case studies, and for the whole DJF 2020/21 season, are available in the supplementary material are weaker negative LGR_p values (where the ensemble is tending to converge in this Lagrangian sense) particularly in the ridge-building region above the northern part of the WCB (see Fig. 1b). Further investigation could help confirm if this is associated with the erosion of the eastern edge of the upper level trough (Ahmadi-Givi et al., 2004), discussed above.

As Fig. 2 but for cyclogenesis Case 1, with the frame centred at 00 UTC on 18 January 2020.

Strong growth-rates are seen at the southern extent of the upper-level trough in The supplementary material includes animations of similar plots to Fig. 2 and Fig. ?. More generally, in the animation for DJF 2020/21, they tend to occur just ahead of the base of the upper-level trough — often preceding cyclogenesis. They also occur within strongly precipitating WCBs. Also evident. They show fields of P_{315} , v_{850} and precipitation which effectively ‘shadow’ the true synoptic evolution of the flow, with LGR_p highlighting the initial ($\sim 12 \text{ h}$) rate of divergence of the ensemble about the synoptic state. Synoptic features associated with large model growth rates are evident. The results in Fig. 2 and Fig. ? are weaker negative growth-rates (where the ensemble is tending to converge) particularly in the ridge-building regions at the head of WCBs. This feature is repeated in numerous cases during the DJF 2020/21 season — a good example being around 2 February 2021. Further investigation of the potential processes discussed above, as in Baumgart and Riemer (2019), would be very valuable. For example, does differential vorticity advection (as in the Omega equation) play an important role in the region at the southern extent of the upper-level trough — either directly through uncertainty in the corresponding adiabatic ascent, or through uncertainties in the potential diabatic feedbacks? Moreover, how well do these modelled growth-rates correspond to the divergence of state trajectories on the real-world attractor? Here, a slightly easier question is first asked: “How well do growth-rates agree amongst the TIGGE models?” are typical of many cases seen within the animations. In addition to these cyclogenesis cases, which

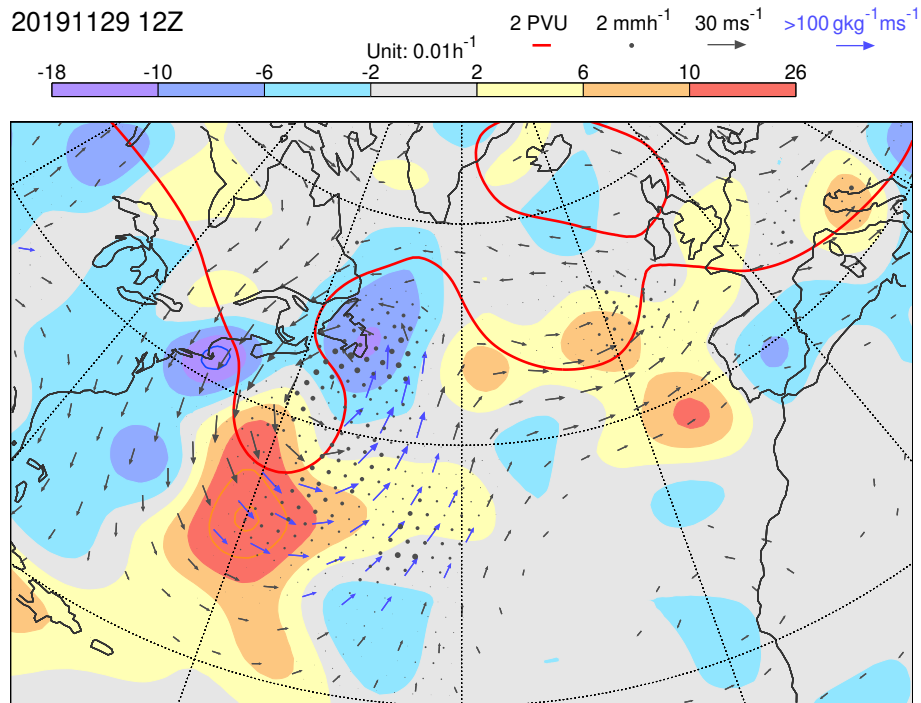


Figure 2. Single frame from the animation of cyclogenesis Case 1 Growth rate LGR_p for P_{315} in the EDA background ensemble forecast forecasts (shaded), focusing on synoptic spatio-temporal scales. The frame is centred at 12 UTC on 29 November 2019. Plotted Note that orange and blue contours extend the shading scheme, with the same interval. In these cases, the most extreme values are indicated at the control forecast $PV_{315} = 2$ ends of the colour bar. Also shown, for the unperturbed EDA member, are $P_{315} = 2$ PVU (red contour) and v_{850} (vectors, which are plotted blue if the moisture flux at 850 hPa exceeds $100\text{gkg}^{-1}\text{ms}^{-1}$), the ensemble mean precipitation (is indicated with black dots, (with radius proportional to the precipitation rate up to the maximum size at 2mmh^{-1}), and. The fields shown are constructed using the ensemble uncertainty growth rate for 12 h background forecasts from the ensemble standard deviation of PV_{315} EDA (shaded so no lead-times are greater than 12 h), as on started at 06 and 18 UTC. Calculations use centred-means and differences between consecutive hourly leadtimes. For the left-hand-side upper tropospheric fields, P_{315} and zonal and meridional winds at $\theta = 315\text{K}$ (u_{315} and v_{315}) are first interpolated to an “N32” reduced Gaussian grid (with 32 latitudes between the pole and equator). The spatial derivatives within the advection term in LGR_p are calculated using spectral transforms to and from a “T42” spherical harmonic representation. Note that N32 is sufficient to avoid aliasing of Eq higher harmonics of the quadratic advection term into the T42 representation. The 12 fields of P_{315} and LGR_p are then concatenated over EDA cycles and spatially smoothed with a synoptic spatio-temporal filter (?? details in main text). Contours extend the shading scheme The resulting timeseries of fields can be used to produce animations of P_{315} which ‘shadow’ the most extreme values true synoptic evolution of the flow, which are indicated with LGR_p highlighting the initial ($\sim 12\text{h}$) rate of divergence of the ensemble about the synoptic state. For the lower-tropospheric fields shown, zonal and meridional winds and specific humidities at 850 hPa (u_{315} , v_{315} , q_{850}) and surface pressure p_* , all from the ends-background forecasts of the colour bar control EDA member, are first interpolated to an “O32” octahedral reduced Gaussian grid (with 32 latitudes between the pole and equator). Further details Values are available in set to “missing” where the main-text 850 hPa surface is below the land surface (where $p_* < 850\text{hPa}$) and in Appendix ?? the moisture flux is calculated as $q_{850}\sqrt{u_{850}^2 + v_{850}^2}$. The ensemble mean total precipitation rate is used to indicate where precipitation is likely to occur. This is obtained on a higher resolution “O80” octahedral grid to give a good symbolic representation (stippling) of rainfall. After similar concatenation of EDA cycles, the 13

often include strongly precipitating WCBs (with embedded convection, Oertel et al., 2020), other common situations for strong growth rates (not investigated here, but consistent with previous studies) are during the extratropical transitions of tropical cyclones (Riemer and Jones, 2014), and within high CAPE situations over North America where mesoscale convection is likely to develop (Rodwell et al., 2013; Sun and Zhang, 2016; Rodwell et al., 2018). All of these situations can lead to deterministic forecast ‘busts’ or ‘dropouts’ (Lillo and Parsons, 2017), extreme precipitation (Grams and Blumer, 2015) or blocking events (Rodwell et al., 2013) over Europe.

3.1 Uncertainty growth in TIGGE forecasts

As discussed in Sect. 3.1, there are reasons why the growth rates displayed by the ECMWF model within its operational EDA might not agree with intrinsic growth rates associated with the atmosphere’s sensitivity to small scale perturbations. The question arises as to how well the ECMWF growth rates agree with the growth rates derived from the ensembles of other operational forecast centres? This question is explored using the first 12 h of ensemble forecasts within the TIGGE archive, for the models summarised in Sect. 2.2. Since potential vorticity is not archived-available in TIGGE, ~~Z250-uncertainty-growth-rates-are-calculated-instead~~, the pragmatic decision is made to calculate the Lagrangian growth rate $LGR_z = \hat{\sigma}_z^{-1}(\partial\hat{\sigma}_z/\partial t + \bar{v} \cdot \nabla_p \hat{\sigma}_z)$ for $Z = Z250$, the geopotential height field at 250 hPa, where ∇_p is the horizontal gradient operator on the pressure surface.

Figure 3 shows filtered LGR_z (shaded) for the TIGGE models centred on the same time as that shown in Fig. 3 and 2. The caption to Fig. ?? show the corresponding frames from animations based on the concatenation of 12 h forecasts from the four TIGGE models. For the ECMWF model, the 3 provides technical details of the calculation of LGR_z . Other fields shown are the same as in Fig. 2 except that ~~Z250-growth-rates~~ (panels a) there is reasonable agreement with the ~~PV315-growth-rates~~ in is contoured in green. For ECMWF in the region of cyclogenesis, filtered LGR_z from the ENS (Fig. 3a) agrees quantitatively quite well with filtered LGR_p from the EDA (Fig. 2 and), despite being growth rates of different fields, and despite the use of additional singular vector perturbations in the ENS. One difference of note for later might be that the maximum ENS growth rate is placed a little more towards the western side of the upper level trough than is the case for the EDA growth rate (cf Fig. ??). The animation for the whole DJF 2021 season, also available in the supplementary material, displays numerous cyclogenesis events and suggests that all four models tend to enhance growth rates at the southern extent of upper-level troughs. Nevertheless, differences between the 2, Fig. 3a).

Comparison amongst the models in Fig. 3 indicates strong agreement, over the first 12 h, in their portrayal of the synoptic situation, as displayed in the fields of ~~Z250, v850, moisture fluxes~~ and, to some extent, precipitation. Although there are commonalities, such as in the observational information available to each centre’s data assimilation, this agreement suggests that the short range forecasts of all models ~~in their uncertainty growth rates are very evident in shadow~~ well the true synoptic evolution. Despite this agreement, the filtered LGR_z differs widely amongst the models in this example. Looking over many examples (within the TIGGE animation for the DJF 2020/21 season in the supplementary material), the agreement can be better (Fig. 3 and Fig. ??, despite very similar upper-level height fields, low-level winds and precipitation. In particular, 4). Nevertheless, differences between the models’ growth rates can be striking, with the ECMWF model ~~tends-tending~~ to display the strongest ~~growth-rates~~-values. The question arises as to whether the ECMWF growth rates are too strong in the vicinity of

cyclogenesis? Is the ECMWF ensemble spread being inflated unnecessarily in these situations, with the consequent impact on forecast scores?

355 ~~Clearly differences in~~ The differences in the models' filtered LGR_z reflect differences in initialisation procedures, differences in the representation of model uncertainty, and differences in the deterministic models themselves ~~will all contribute to the growth-rate differences between the forecast systems. It would be useful to know which is closest to the truth, and why. In an attempt to begin to answer these questions, the next section discusses an extended~~ (summarised in Table 1). While it is difficult to evaluate these growth rates per se, it is possible to assess how well each ensemble system maintains short-range statistical reliability within the North Atlantic stormtrack. This will be done in Sect. 4.1, after considering important conceptual aspects of short-range reliability and introducing a novel spread-error equation which estimates deficiencies in short-range ensemble spread in the face of bias and analysis uncertainty relationship in Sect. 4.1 and 4.2.

4 ~~The “extended spread-error” equation~~

4 Forecast reliability

365 Reliability (Sanders, 1958) is a key attribute of ensemble forecasts (Gneiting and Raftery, 2007), allowing users to make unbiased decisions (Rodwell et al., 2020). The concept of reliability can be understood with reference to the schematic in Fig. 5. For clarity, the figure is shown in two dimensions and could relate, for example, to the prediction of the location of a storm. For a reliable forecast system (Hamill, 2001; Saeltra et al., 2004), the verifying truth T should be statistically indistinguishable from any random sampling of the forecast distribution (Hamill, 2001; Saeltra et al., 2004). ~~A necessary condition of~~ reliability is that, when averaged over many ensemble forecasts, the average difference between the truth and the ensemble F , indicated by the grey concentric circles. This distribution, which need not be Gaussian or even uni-modal, has mean μ_F and standard deviation of distances from the mean σ_F (grey dashed line). Introducing a suffix j to indicate the forecast initiated at time t_j with $j \in \{1, \dots, n\}$ then, since F_j is reliable (and assumed to be the only information available at time t_j about T_j), the expectation $\mathbb{E}_j[\cdot]$ at time t_j is that $\mathbb{E}_j[T_j] = \mu_{F_j}$ and $\mathbb{E}_j[(T_j - \mu_{F_j})^2] = \sigma_{F_j}^2$. The latter condition leads to the common ‘spread-error’ relation in ensemble forecasting — that reliability requires $\overline{(T - \hat{\mu}_F)^2} \approx \overline{\hat{\sigma}_F^2}$, where $\hat{\mu}$ and $\hat{\sigma}$ are the mean and standard deviation estimators, respectively, based on the sample of m ensemble members, and an overline indicates a mean of the n forecasts. Equality here can be improved by accounting for the finiteness of m and increasing n (Leutbecher and Palmer, 2008).

For the short forecast leadtimes of interest here, the spread-error relation is not adequate in general. This is because uncertainties in the knowledge of the verifying truth can be non-negligible compared to forecast variances at short leadtimes. Ensemble data assimilation (such as the EDA at ECMWF discussed in section 2.1) aims to estimate the uncertainty in the knowledge of the truth. A reliable analysis distribution A , which is consistent with the indicated truth T , is shown in Fig. 5 using blue concentric circles, with mean μ_A and standard deviation of distances from the mean (e.g., σ_A (blue dashed line).

Let \tilde{F} and \tilde{A} be the underlying distributions associated with the operational forecast and verifying analysis. These distributions might not be reliable. For example, bias in these distributions could have a non-negligible impact on reliability — their means

20200118 00Z

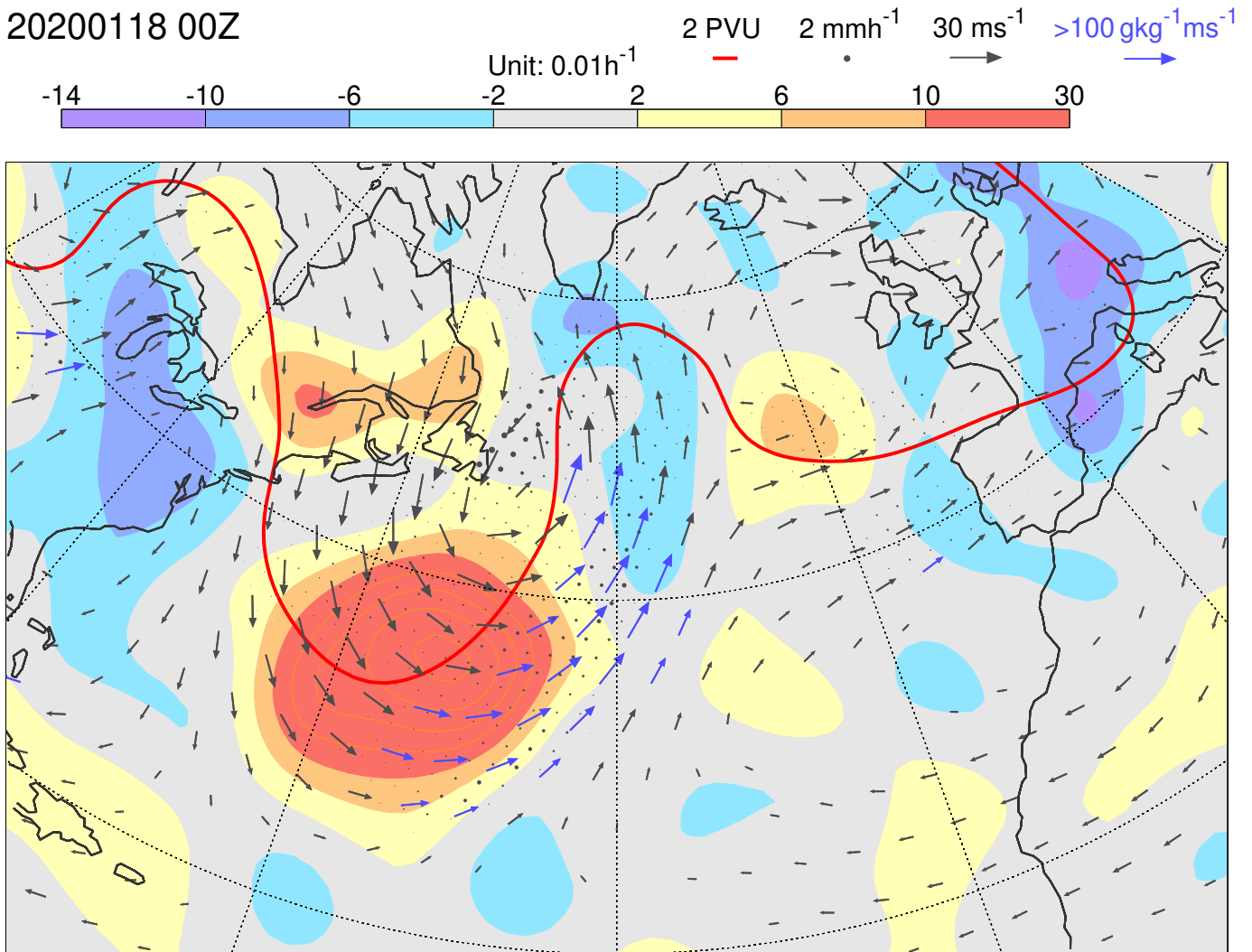
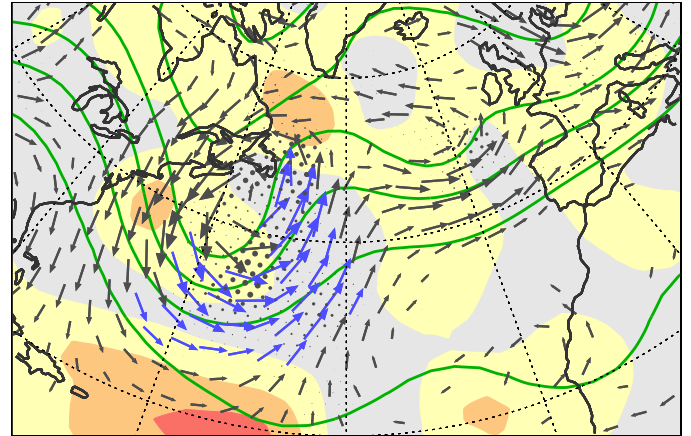
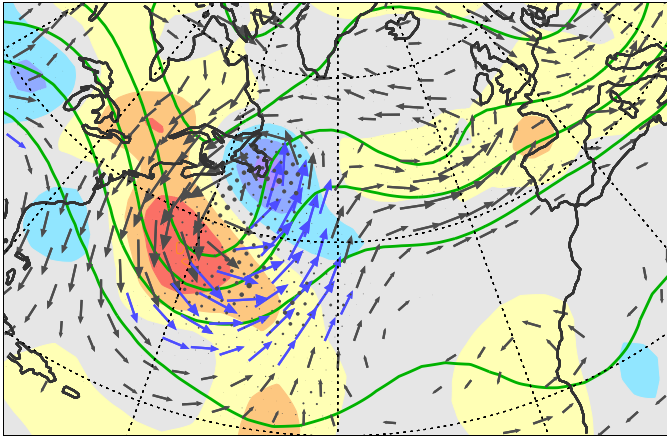


Figure 3. A single frame Growth rate LGR_z for Z250 for TIGGE models (shaded), centred at 12 UTC on 29 November 2019, from an animation of 2019. Note that orange contours extend the cyclogenesis case shading scheme with the same interval, focusing on synoptic spatio-temporal scales where required. In these cases, from (a) ECMWF, (b) JMA, (c) NCEP, and (d) UKMO ensemble forecast data obtained from the TIGGE archive. Plotted most extreme values are indicated at the control forecast ends of the colour bar. Also shown, for the unperturbed ensemble members, are Z250 (green contours) and v_{850} (vectors, which are plotted blue if the moisture flux at 850 hPa exceeds $100 \text{ gkg}^{-1} \text{ ms}^{-1}$), the ensemble mean. Ensemble mean precipitation is indicated with (black dots, with radius proportional to the precipitation rate up to the maximum size at 2 mmh^{-1}). The models shown are from (a) ECMWF, and the ensemble uncertainty growth rate for Z250 (shaded) (b) JMA, (c) NCEP, and (d) UKMO as discussed in Eq Sect. (??) 2.2. Contours extend the shading scheme to the most extreme values, which are indicated at constructed using the ends first 12 h of the colour bar each model's ensemble forecasts started at 00 and 12 UTC. Further Calculations use centred-means and differences between consecutive 6-hourly leadtimes (0 h, 6 h, 12 h). All other details are available in the main text and same as in Appendix ?? the caption to Fig. 2, except that the plotted Z250 field is not spatially smoothed (it is considered already a synoptic scale field). Note that humidity fluxes could not be calculated for the UKMO model as specific humidity data was not available from TIGGE.

(a) ECMWF 20191129 12Z

(b) JMA 20191129 12Z



(c) NCEP 20191129 12Z

(d) UKMO 20191129 12Z

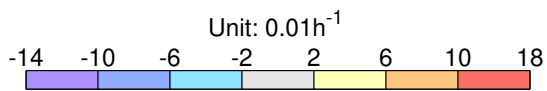
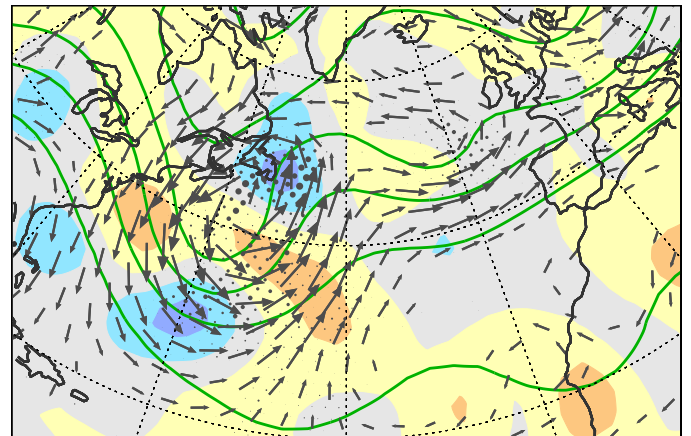
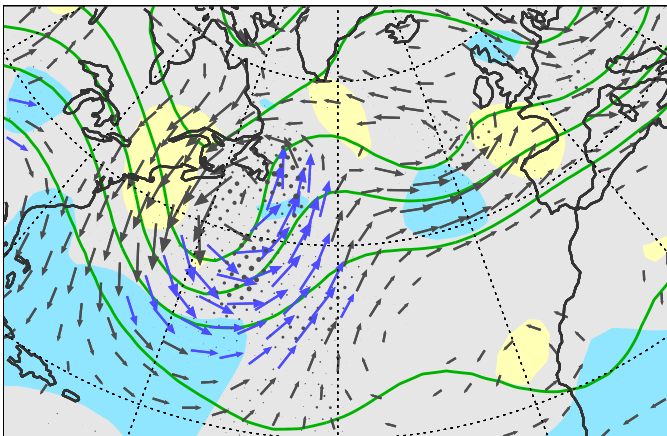


Figure 4. As Fig. 3, but centred at 012 UTC on ~~18-January~~ 8 December 2020. This situation also corresponds to an event of cyclone intensification off the North American east coast associated with a WCB.

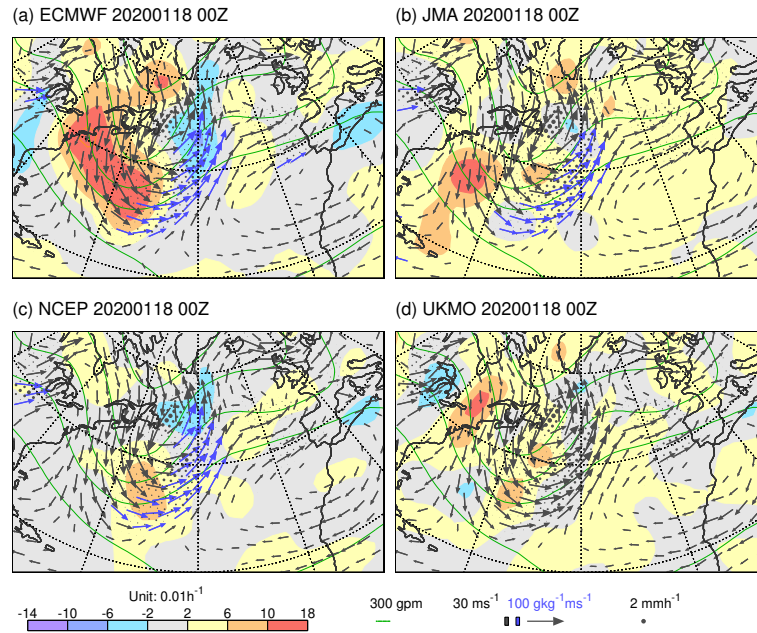


Figure 5. Schematic in 2 dimensions showing the “departure” d as the difference between the ensemble mean of the operational forecast $\hat{\mu}_{\tilde{F}}$ and the ensemble mean of the verifying operational analysis $\hat{\mu}_{\tilde{A}}$. The forecast and analysis ensembles can be considered as finite samplings of the underlying distributions with (mean,variance) = $(\mu_{\tilde{F}}, \sigma_{\tilde{F}}^2)$ and $(\mu_{\tilde{A}}, \sigma_{\tilde{A}}^2)$, respectively. Circles depict the hypothetical forecast and analysis distributions with (mean,variance) = (μ_F, σ_F^2) and (μ_A, σ_A^2) , respectively, that would be created with a perfect model (and imperfect/incomplete observational information). The truth is indicated with a T .

$\mu_{\tilde{F}}$ and $\mu_{\tilde{A}}$, respectively, are shown offset from those of the reliable distributions in Fig. 5. The ensemble (sample) means of these distributions are indicated by $\hat{\mu}_{\tilde{F}}$ and $\hat{\mu}_{\tilde{A}}$. These latter two parameters, along with their difference (or ‘departure’) d , are the only parameters shown in Fig. 5 that are ascertainable here, being obtained from the operational ensemble forecast system. Perhaps more importantly for reliability, the distributions \tilde{F} and \tilde{A} could have deficiencies in their variances $\sigma_{\tilde{F}}^2$ and $\sigma_{\tilde{A}}^2$, respectively. Are they under-spread or over-spread with respect to the variances of the reliable distributions, for example? Again, it is only the ensemble sample estimators $\hat{\sigma}_{\tilde{F}}^2$ and $\hat{\sigma}_{\tilde{A}}^2$ that are ascertainable here.

For the interested reader, Sect. 4.1 gives a derivation of an extended spread–error equation, which takes bias, analysis uncertainty and sampling into account in the mean–squared–error of the ensemble–mean) should match the average difference between an ensemble member and the ensemble mean (e. g., the ensemble variance). This is the so–called “evaluation of ensemble spread. Salient aspects of this extended spread–error equation”. In the present study, this equation is extended to account for bias and analysis uncertainty (uncertainty in our knowledge of the truth), which can be non–negligible at the short lead–times considered, in an “extended spread–error equation” equation are discussed in Sect. 4.2.

4.1 Derivation of the extended spread–error equation

400 For initial time t_j , the departure of the ensemble mean forecast $\widehat{\mu}_{\widetilde{F}_j}$ from the ensemble mean analysis $\widehat{\mu}_{\widetilde{A}_j}$ can be written (by following the other solid blue lines in Fig. 5) as:

$$\begin{aligned}
 d_j &= (\widehat{\mu}_{\widetilde{F}_j} - \widehat{\mu}_{\widetilde{A}_j}) \\
 &= (\widehat{\mu}_{\widetilde{F}_j} - \mu_{\widetilde{F}_j}) + (\mu_{\widetilde{F}_j} - \mu_{F_j}) + (\mu_{F_j} - T_j) + (T_j - \mu_{A_j}) + (\mu_{A_j} - \mu_{\widetilde{A}_j}) + (\mu_{\widetilde{A}_j} - \widehat{\mu}_{\widetilde{A}_j}) \\
 &= \underbrace{(\mu_{F_j} - T_j)}_1 + \underbrace{(\widehat{\mu}_{\widetilde{F}_j} - \mu_{\widetilde{F}_j})}_2 + \underbrace{(T_j - \mu_{A_j})}_3 + \underbrace{(\mu_{\widetilde{A}_j} - \widehat{\mu}_{\widetilde{A}_j})}_4 + \underbrace{(\mu_{\widetilde{F}_j} - \mu_{F_j})}_5 + \underbrace{(\mu_{A_j} - \mu_{\widetilde{A}_j})}_6,
 \end{aligned} \tag{4}$$

An-overline where the last line is just a convenient re-arrangement of the terms on the second line.

405 As discussed above, the terms 1–6 in Eq. (9) represents a mean over ensemble forecast start times. The schematic in Fig. 5 shows the salient aspects of 4) would be difficult to quantify in the operational forecast system because they require knowledge of the truth and the moments of the underlying distributions (only d_j , $\widehat{\mu}_{\widetilde{F}_j}$ and $\widehat{\mu}_{\widetilde{A}_j}$ are quantifiable). Nevertheless, we can discuss their expected values. The expectation operator $\mathbb{E}_j[\cdot]$, introduced above, is the expectation for a given initial time t_j . The forecast distributions F_j and \widetilde{F}_j are fixed for given initial time, so the expectation \mathbb{E}_j is over the potential T_j (with distribution F_j) and the potential analysis distributions A_j and \widetilde{A}_j (which are dependent on T_j). The expectation is also over the finite ensemble samplings \widehat{F}_j of \widetilde{F}_j and \widehat{A}_j of \widetilde{A}_j .

410 The reliability of $A_j(T_j)$ implies that $\mathbb{E}_j[T_j] = \mathbb{E}_j[\mu_{A_j}] (= \mu_{F_j})$ and $\mathbb{E}_j[(T_j - \mu_{A_j})^2] = \mathbb{E}_j[\sigma_{A_j}^2]$. Taking the expectation of the last line in Eq. (9) for a single start time. An ensemble is considered to be a finite sampling of an “underlying distribution”. The ensemble-mean forecast is shown as $\widehat{\mu}_{\widetilde{F}_j}$, where a hat indicates that this is an estimator of 4) we have:

$$\mathbb{E}_j[d_j] = \mathbb{E}_j[\mathbf{5} + \mathbf{6}] = \mathbb{E}_j \left[(\mu_{\widetilde{F}_j} - \mu_{F_j}) - (\mu_{\widetilde{A}_j} - \mu_{A_j}) \right] \equiv \beta_{\widetilde{F}_j} - \beta_{\widetilde{A}_j} \equiv \beta_j, \tag{5}$$

415 since terms 1–4 in Eq. (4) have zero expectation. Hence $\mathbb{E}_j[d_j] = \beta_j$: the expected bias of the unreliable forecast $\beta_{\widetilde{F}_j}$ minus the expected bias of the unreliable analysis $\beta_{\widetilde{A}_j}$. As lead-time increases, one might expect that the forecast bias will become the dominant component of β_j .

The extended spread-error equation is based on the expected square of Eq. (4). This involves squared terms, such as $\mathbb{E}_j[\mathbf{1} \cdot \mathbf{1}]$, and cross terms, such as $2\mathbb{E}_j[\mathbf{1} \cdot \mathbf{6}]$. With the squared terms presented in the same order as in the last line in Eq. (4) the expected square of Eq. (4) can be written as:

$$\begin{aligned}
 \mathbb{E}_j[d_j^2] &= \sigma_{\widetilde{F}_j}^2 + \frac{1}{m} \sigma_{\widetilde{F}_j}^2 + \sigma_{A_j}^2 + \frac{1}{m} \sigma_{A_j}^2 + (\beta_{\widetilde{F}_j} - \beta_{\widetilde{A}_j})^2 + \mathcal{E}_j \\
 &= \frac{m+1}{m} (\sigma_{\widetilde{F}_j}^2 + \sigma_{A_j}^2) + \beta_j^2 + \underbrace{\left\{ (\sigma_{F_j}^2 - \sigma_{\widetilde{F}_j}^2) + (\sigma_{A_j}^2 - \sigma_{\widetilde{A}_j}^2) + \mathcal{E}_j \right\}}_{\text{Variance deficit}}.
 \end{aligned} \tag{6}$$

The term in parentheses $\{ \}$ comprises the “variance deficit” (which compares the reliable and unreliable variances of the ensemble forecast and analysis) and \mathcal{E}_j , which collects any potentially non-zero cross terms and the mean $\mu_{\hat{F}}$ of the underlying forecast distribution, and a tilde indicates that the forecast is made with an imperfect model. Similarly, the ensemble-mean analysis $\hat{\mu}_A$ is an estimator (expected) variance in analysis bias (see later for further discussion).

425 From Eq. (6), the expected squared departure (over an infinite set of initial forecast times t_j) can then be written as

$$\mathbb{E}[d^2] = \frac{m+1}{m} \mathbb{E}[\sigma_F^2 + \sigma_A^2] + \mathbb{E}[\beta]^2 + \mathbb{E}[R] \quad , \quad (7)$$

with expected “residual”:

$$\mathbb{E}[R] = \mathbb{E} \left[(\sigma_F^2 - \sigma_{\hat{F}}^2) + (\sigma_A^2 - \sigma_{\hat{A}}^2) \right] + \mathbb{E}[\mathcal{E}] + \sigma_{\beta}^2 \quad , \quad (8)$$

430 where the variance in forecast bias $\sigma_{\beta}^2 = \mathbb{V}[\beta]$ accounts for the explicit replacement of $\mathbb{E}[\beta^2]$ with $\mathbb{E}[\beta]^2$ in Eq. (7). It can be seen that all terms that involve variations in bias have been moved into the residual.

For an unbiased estimator of Eq. (7), we note that $(\mathbb{E}[d^2] - \mathbb{E}[\beta]^2) = (\mathbb{E}[d^2] - \mathbb{E}[d]^2) = \mathbb{V}[d]$ which has unbiased estimator $\frac{n}{n-1} (\bar{d}^2 - \bar{d}^2)$, and obtain the extended spread-error equation:

$$\frac{n}{n-1} \bar{d}^2 = \frac{m+1}{m-1} \overline{(\hat{\sigma}_F^2 + \hat{\sigma}_A^2)} + \frac{n}{n-1} \bar{d}^2 + \bar{R} \quad , \quad (9)$$

Error² Spread² AnUnc² Bias² Residual⁽²⁾

435 where the various terms have been named for future reference. For the purposes of calculating statistical significance, \bar{R} is written as the mean of the mean $\mu_{\hat{A}}$ of the underlying analysis distribution. The line labelled d represents the departure of the ensemble-mean forecast from the ensemble-mean analysis $\hat{\mu}_{\hat{F}} - \hat{\mu}_{\hat{A}}$ residuals R_j :

$$R_j \equiv \frac{n}{n-1} (d_j^2 - \bar{d}^2) - \frac{m+1}{m-1} (\hat{\sigma}_{Fj}^2 + \hat{\sigma}_{Aj}^2) \quad , \quad (10)$$

440 which close the budget for each initial time (for given, constant \bar{d}). The extent to which \bar{R} is a good estimate for the expected “variance deficit” in Eq. (8) will depend on the magnitude of the other terms $\mathbb{E}[\mathcal{E}] + \sigma_{\beta}^2$ in Eq. (8). In Appendix A, it is suggested that the only term that could be non-negligible is the variance in forecast bias, σ_{β}^2 .

4.2 Summary of the extended spread-error equation

The Error² term in Eq. (9) is the scaled mean-square of these departures mean square of the departures d . (Scaling ensures factors within each term ensure that the equation is unbiased with a finite valid for any number of forecasts n and finite

ensemble size m). The extended spread-error equation ($n > 1$ and any ensemble size $m > 1$), Eq. (9) aims to relate ~~writes the~~
 445 Error² to ~~as~~ the sum of the ~~mean-squares of the other lines in Fig. 5. This is derived fully in the Appendix ??.~~ The resulting
~~mean estimated forecast variance (Spread² and), mean estimated analysis variance (AnUnc² (analysis uncertainty) terms involve~~
~~the variance estimators $\hat{\sigma}_F^2$ and $\hat{\sigma}_A^2$ of the forecast and analysis distributions, respectively. The Bias² is the squared-mean of the~~
~~departures (the square of the), squared estimated mean bias). The (Bias²) and the Residual⁽²⁾ is the mean of the residuals that~~
~~close the budget for each initial time (assuming constant bias). The . This final term simply closes the budget — the~~ superscript
 450 ⁽²⁾ signifies that ~~this Residual⁽²⁾ is also in squared units, although it can be negative as well as positive. For the purpose of~~
~~statistical significance testing, Residual⁽²⁾ can be written as a mean of residuals Eq.(10), which close the budget for each initial~~
~~time (assuming constant bias).~~

Schematic in 2 dimensions showing the “departure” d as the difference between the ensemble-mean of the operational
 forecast $\hat{\mu}_F$ and the ensemble-mean of the verifying operational analysis $\hat{\mu}_A$. The forecast and analysis ensembles can be
 455 considered as finite samplings of the underlying distributions with (mean, variance) = (μ_F, σ_F^2) and (μ_A, σ_A^2) , respectively.
 Circles depict the hypothetical forecast and analysis distributions with (mean, variance) = (μ_F, σ_F^2) and (μ_A, σ_A^2) , respectively,
 that would be created with a perfect model (and imperfect/incomplete observational information). The truth is indicated with a
 T .

If the mean ~~If~~ Bias \bar{d} is different from zero ~~at some level of significance (here 5% with a t-test)~~, then this indicates a bias
 460 in the mean of the underlying forecast distributions relative to ~~those of a perfect model ($\mu_F - \mu_F$) or a bias in the mean of~~
~~the that of the~~ underlying analysis distributions ~~relative to those made using a perfect model ($\mu_A - \mu_A$).~~ Similarly, if the
 Residual⁽²⁾ ~~is different from zero at some level of significance, then this generally indicates a deficiency in the variance of the~~
~~underlying forecast and/or analysis distribution. (estimates the sum of the deficits in forecast and analysis variance, plus the~~
~~(potentially non-negligible) temporal variance in forecast bias.~~ A negative Residual⁽²⁾ indicates a surplus in variance, while
 465 positive values ~~can~~ indicate a deficit in variance provided the ~~main additional term in the Residual⁽²⁾ — the~~ variance of forecast
 bias ~~— is negligible or accounted for; see later. Hence, if either Bias or Residual⁽²⁾ differ from zero, then this indicates a lack~~
 of reliability in either the first or second moments of the forecast or analysis distributions. As ~~lead-time~~ ~~lead-time~~ increases,
 one might expect the issues in the forecast distribution to begin to dominate.

For display purposes the terms in Eq. (9) can be put into more understandable units by taking their ~~square-roots~~ ~~square-roots~~
 470 — signified by removing the superscript ~~2-label.~~ ² label. This approach leaves the bias in its correct form, for example.
 Since \bar{R} can be positive or negative, “Residual” = $\sqrt{|\bar{R}|} \cdot \text{SGN}(\bar{R})$ is plotted to retain the sign. ~~One should be aware that the~~
~~square-rooting will tend to make smaller terms~~ ~~While smaller terms will~~ look more important than they ~~really~~ are in the ~~proper~~
~~(squared-) budget~~ ~~squared budget, the residual still correctly indicates spread deficiencies.~~ Statistical significance is determined
~~from the un-rooted (at the 5% level with a t-test) from the un-rooted~~ terms (except for Bias², which must be determined in its
 475 ~~non-squared~~ ~~non-squared~~ form).

As an aside, a very similar equation to Eq. (9) was presented by Rodwell et al. (2016) for application in “observation space”.
 That equation represents a more fundamental “ideal” where ~~assigned~~ observation error variances are ~~assigned~~ ~~assumed~~ to
 represent their true values. In reality, these ~~observation error variances~~ can be inflated to account for representativeness error

(Rennie et al., 2021), observation error correlations, or when associated with ~~non-linear~~ non-linear observation operators. This
480 can mean that the budget will not balance for a given observation type, even if the resulting analyses and forecasts are reliable
in “model space”. Hence the current model space application represents a complementary approach, which can be more readily
applied to a range of models and ~~lead-times~~ lead-times, and which can be used to assess ensemble initialisation aspects.

5 ~~Seasonal-means-of-the-extended-spread-error-equation~~

4.1 Seasonal mean forecast reliability in the TIGGE ensembles

485 Figure 6 shows the (~~square-rooted~~ square-rooted) terms of the extended spread-error ~~equation-Eq. (9)~~ for Z250 based on all
day-2 ensemble forecasts verifying in DJF 2020/21 from the ECMWF (top ~~)-and-UK-Met-Office-(middle)ensembles,-and-the~~
~~differences-(bottom-row)~~, JMA (second row), NCEP (third row) and the UK Met Office (bottom row) ensembles. Focusing
first on ECMWF (top), the North Atlantic winter stormtrack is evident as a region of enhanced ensemble spread (Fig. 6b).
Even without the AnUnc and Bias contributions, the Spread is larger than required to balance the Error (Fig. 6a) — signifying
490 “~~over-spread~~ over-spread” in the stormtrack at day 2. Analysis uncertainty is also enhanced in the stormtrack region (Fig. 6c)
and a statistically significant Bias is seen over the east coast of North America. Confirmation of the ~~over-spread~~ over-spread is
seen with the large negative Residual (Fig. 6e). Note the different ~~colour-bar~~ colour-bar convention for the Bias and Residual,
which can take positive and negative values. Over the North American east coast, the squared budget Eq. (9) is roughly
 $15^2 = 18^2 + 3^2 + 6^2 - 12^2 \text{ m}^2$. Because AnUnc and Bias are not negligible here, the ~~reliable-Spread~~ ‘reliable Spread’ (i.e.,
495 ~~Spread-in-case-of~~ the Spread required for a zero Residual) in this region would actually be $\sim 13.4^2 \text{ m}^2$, somewhat less than the
 15^2 m^2 which might be inferred from the standard spread-error relationship. Accounting for the variance of forecast bias (which
is difficult to estimate here but see later) would further reduce the reliable Spread a little. In contrast, there is a positive Residual
over the subtropical North Atlantic (Fig. 6e). Whether this indicates insufficient Spread to account for the elevated Errors in this
region (Fig. 6a) or is associated with variance in forecast bias is also discussed later. Note that Rodwell et al. (2018) indicated
500 better reliability for this model. Partly this reflects compensation in their annual and hemispheric means, partly it reflects the
importance (here) of accounting for bias and analysis uncertainty, and partly it reflects a recent deterioration in stormtrack
reliability.

~~The corresponding budget for the UKMO (middle row of panels) also indicates an over-spread in the stormtrack at day~~
~~2-(For the JMA ensemble during this season, day-2 Error is larger than for ECMWF (cf Fig. 6j), but by a smaller degree.~~
505 ~~The difference plots (bottom row of panels) show that Error, AnUnc and |Bias| are all generally smaller for ECMWF (a,f),~~
~~and the Spread is increased by a larger amount (cf Fig. 6b,g). Note that mean values and root-mean-square (RMS) values,~~
~~integrated over the area shown, are indicated above each panel in Fig. 6 — it is the RMS values which are most appropriate~~
~~for comparison. AnUnc and Bias are also larger for JMA (cf Fig. 6k,c,h and d,i). Consequently, the residual is more strongly~~
~~negative (cf Fig. 6m,e,j) — indicating more severe over-spread in this ensemble at this leadtime. For the NCEP ensemble~~
510 ~~relative to ECMWF, a smaller increase in Spread (cf Fig. 6n). In particular, ECMWF starts from a somewhat sharper analysis~~
~~distribution outside the stormtrack region. However, ECMWF forecast Spread grows more rapidly in the stormtrack, and results~~

in a stronger |Residual| than for the UKMO (b,l) than in Error (cf Fig. 6a,k) leads to better variance reliability (cf Fig. 6e,o), despite having larger AnUnc and Bias (cf Fig. 6o).

Note that the over-spread aspect is not specific to Z250 or the North Atlantic. Supplementary Figure ?? and c,m and d,n).
515 For the UKMO ensemble relative to ECMWF, Error is larger (cf Fig. 6a,p) and Spread is reduced (cf Fig. 6b,q) — leading to the best variance reliability of the four models (Fig. 6t); again despite having larger AnUnc and Bias (cf Fig. ?? show that similar conclusions can be drawn for the more commonly verified field of geopotential heights 6c,r and d,s) than for ECMWF. Note that conclusions drawn in this section appear to generalise to other parameters (such as geopotential heights and temperatures at 500hPa in all the northern and southern hemispheric stormtracks in DJF 2020/21 and June — August 2021 (JJA 2021). The UKMO ensemble appears particularly over-spread in polar regions. Note that these supplementary figures show the non-rooted terms to give a better impression of the relative contributions to the overall budget in Eq. (9) — hPa), other seasons, other stormtracks, and continue until the most recent check for the March — May season 2022 (not shown). Using these four models as a demonstration of what could be possible in day 2 ensemble forecasts for the North Atlantic stormtrack, the conclusion would be to pick the errors, analysis uncertainties and bias of the ECMWF model, and the spread and reliability
525 of the UKMO model. With reference to Table 1, an interesting commonality of the two most over-spread systems (ECMWF and JMA) is the use of singular vector perturbations in their initial conditions. Puzzlingly, however, JMA appears to show the weakest initial growth rates.

A key question for this study is whether the ECMWF Residual (So, a partial answer to the question in Sect. 3.1 is yes, initial growth rates in the ECMWF ensemble do seem to be too strong within the winter North Atlantic stormtrack. To fully
530 answer the question, it needs to be determined whether the negative Residual in Fig. 6e) is associated with a general level of over-spread (e.g. associated with uncertainties in large-scale waves Durran and Gingrich, 2014), over-spread or whether it is associated with difficulties in modelling particular flow evolutions, such as cyclogenesis ? This question will be addressed based on a clustering of the can be linked to cyclogenesis events per se? The aim now is to address this question by clustering the stormtrack flow configurations in DJF 2020/21. In the next section, the method of clustering is discussed.

535 5 Flow-type clustering

4.1 Compositing cases of cyclogenesis in the ECMWF ensemble

The method of aim is to obtain a cyclogenesis/non-cyclogenesis partition of the 12 hourly analysed synoptic flow within the DJF 2020/21 season. The method used is K-means clustering (Hartigan and Wong, 1979) is used — means clustering (Hartigan and Wong, 1979), which seeks to minimise the sum of squared deviations from the relevant cluster-mean. It is used here to obtain three flow clusters in a prescribed region of the North Atlantic stormtrack. The data used within the clustering come from the ECMWF forecasts initialized at 00 and 12 UTC, with Z250, and zonal and meridional wind at 850 hPa (u_{850} , v_{850}) at step 0 from the control forecast during DJF 2020/21, and ensemble-mean ensemble mean 12 h accumulated total precipitation from the previous forecast (so the end of the accumulation period corresponds to the time of the circulation fields). It is thought that these fields should be able to capture upper-tropospheric upper-tropospheric Rossby waves, baroclinic structures and associated

performed and the same minimum sum of squared deviations from the cluster-means was generally found within the first 5
555 such initialisations — indicating that the ~~optimal clusters have been identified~~ solution is optimal.

The first clustering region is located at the head of the North Atlantic stormtrack [80°–50°W, 30°–50°N] and contains 11×7 data points on the F32 grid. The rationale for choosing this region is that it corresponds to the North Atlantic “hot spot” for cyclone intensification (e.g. Wernli and Schwierz, 2006) and ~~warm conveyor belt~~ WCB activity (Madonna et al., 2014), and its size corresponds to a ~~half-wavelength~~ half-wavelength of a typical baroclinic wave. Figure 7 (top row) shows
560 the same fields as in Fig. 3 ~~and Fig. ??~~ but averaged over the three sets of date/times obtained from the ~~K-means~~ means clustering in this (indicated) region. Cluster 1 (Fig. 7a, 32 date/times) appears to capture a ~~partially-evolved cyclogenesis flow-type~~ partially-evolved cyclogenesis flow-type off the east coast of North America, with a baroclinic westward tilt with height, intense horizontal moisture flux and precipitation ahead. ~~Strong uncertainty growth-rate~~ A general tendency for strong uncertainty growth rate at the southern extent of the ~~upper-level~~ upper-level trough is also evident. (Note that the ~~growth-rate~~ growth rate is not used within the clustering algorithm since this ~~is what will be evaluated~~ could potentially bias the reliability assessment). Cluster 2 (Fig. 7b, 75 date/times) shows a broader trough, weaker moisture flux, and possible cyclogenesis, displaced further downstream. Cluster 3 (Fig. 7c, 73 date/times) shows a diffuse ridge with a trough even further downstream, and a surface anticyclone in the subtropical western North Atlantic.

~~A~~ To identify cyclogenesis events further downstream in the stormtrack, a second clustering region is displaced ~~north-eastward~~ along the stormtrack north-eastward to [65°–35°W, 35°–55°N] ~~and~~. This region also contains 11×7 data points. Clustering results for this region are shown Fig. ~~???~~ ??? (bottom row). Cluster 1 (Fig. ~~??a~~ 7d, 62 date/times) highlights further cyclogenesis with a closed ~~cluster-mean~~ cluster-mean circulation at 850 hPa over Newfoundland and with strong ~~growth-rates~~ growth rates. Note that, as might be expected, 44 of these 62 date/times (71%) were in cluster 2 for region 1 (Fig. 7b).

~~In total,~~ By combining the two cyclogenesis clusters (Fig. 7a and Fig. 7d), a total of 91 date/times were identified as cyclogenesis flow-types flow-types (32+62 minus 3 duplicates). For each of these date/times (and their 180-91=89 counterpart date/times), visual inspection of plots similar to those ~~for the two case studies (in Fig. 1)~~ suggests that the objective clustering has been successful in partitioning the date/times into cyclogenesis and ~~non-cyclogenesis flow-types~~ non-cyclogenesis flow-types. This then allows the evaluation of the extended spread-error budget for a large set of cyclogenesis events and of the counterpart set.

580 ~~As Fig. 7 but for clustering in the second region (again indicated by a black border):~~

5 ~~The extended spread-error equation for cyclogenesis flow-types~~

4.1 ~~Forecast reliability during cyclogenesis in the ECMWF ensemble~~

Because Fig. 7a and Fig. ~~??a~~ 7d show partially evolved cyclogenesis ~~flow-types~~ flow-types, it is necessary to ~~wind-back~~ wind-back the date/times a little to evaluate the day–2 extended spread-error budget during cyclogenesis. Winding back by one
585 and two days gives very similar results (not shown). Also, conclusions are very similar for the evaluation based on the date/times obtained for the first region alone; albeit with the impact more confined to the ~~head~~ western end of the stormtrack. Here, results

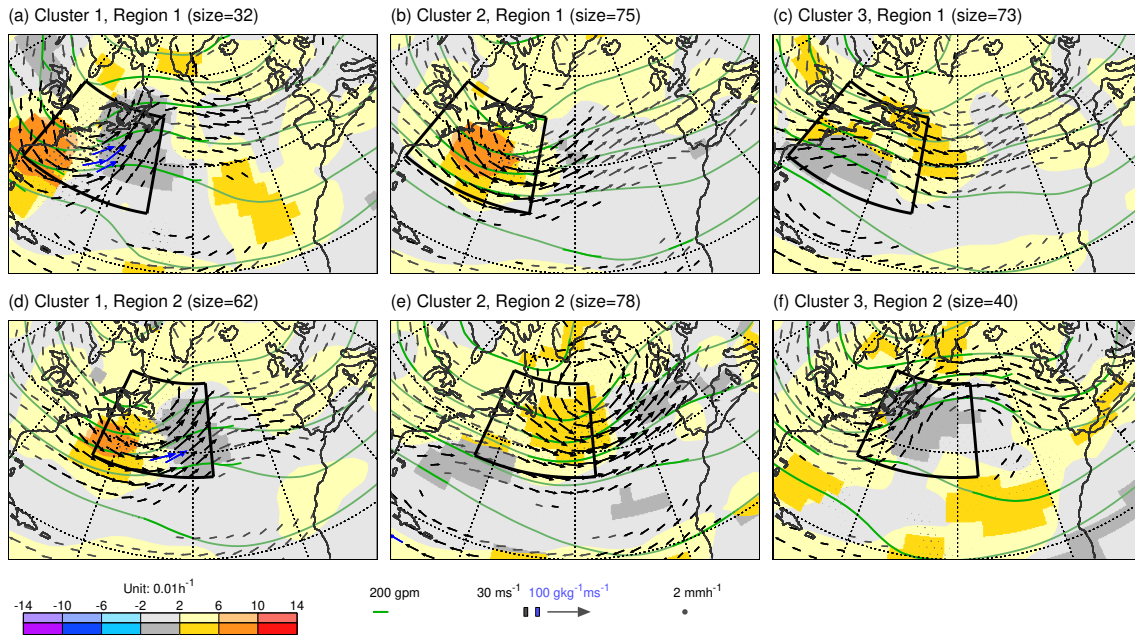


Figure 7. Means over the date/times for each cluster the three clusters obtained from K-means-means clustering in the black-bordered first (top) and second (bottom) region on the fields of Z250 (contours), u_{850} and v_{850} (vectors) from ECMWF control (unperturbed) forecasts at step 0, and ensemble-mean ensemble mean 12h accumulated precipitation (dots) valid (or end of accumulation) at 00 and 12 UTC within the period DJF 2020/21. The two clustering regions are indicated by the black borders in each panel. Although not used in the clustering, shading shows the corresponding mean 12h uncertainty growth-rate Eq. (??) growth rate LGR_Z for Z250. Vectors are coloured blue when the humidity flux at 850 hPa exceeds $100 \text{ gkg}^{-1} \text{ m s}^{-1}$. More saturated shading, contours and vectors and dots indicate statistical significance at the 5% level (not accounting for autocorrelation due to the discontinuous nature of date/times in each cluster).

are shown for a 2-day wind-back (consistent with the time for moderate deepening of a low-pressure system; Wernli and Davies, 1997) (consistent with the time for moderate deepening of a low-pressure system; Wernli and Davies, 1997) and for both regions together. This means that the combined 91+89=180 date/times of the cyclogenesis and counterpart composites represent the same
 590 initial date/times a 91:89 partition (nearly 50:50) of the data used in Fig. 6 (top row).

Figure 8 shows the (square-roots square-roots) of the terms in the extended spread-error equation Eq. (9) for Z250 at day 2 in the ECMWF ensemble, separately for cyclogenesis (top) and counterpart (middle) composites, and their difference (bottom). The black border indicates the union of the two clustering regions. Comparison shows that ensemble spread for the cyclogenesis composite (Fig. 8b) is enhanced around the head in the western part of the North Atlantic stormtrack while the spread for the counterpart composite (Fig. 8g) is centred more downstream. There are also corresponding differences in analysis uncertainty (Fig. 8c and Fig. 8h), possibly due to differing uncertainty growth-rates growth rates in the background forecasts used within the ensemble data assimilation process.

(a) Cluster 1, Region 1 (size=32)

(b) Cluster 2, Region 1 (size=75)

(c) Cluster 3, Region 1 (size=73)

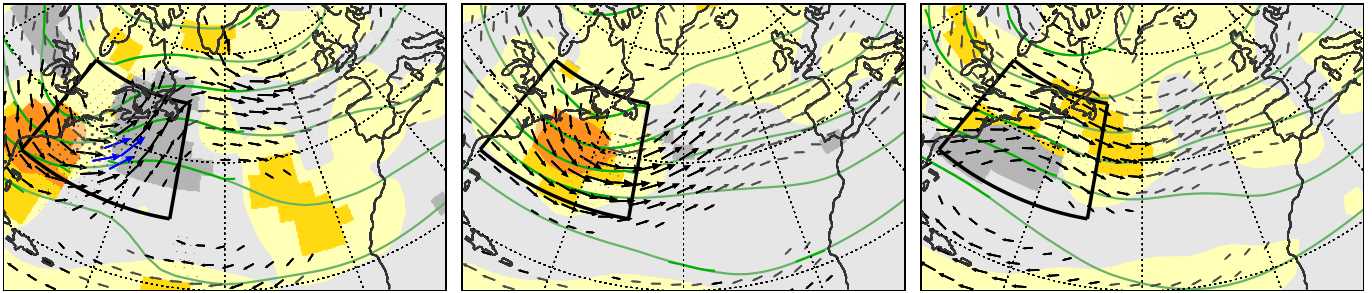


Figure 8. As Fig. 6 but separately for the cyclogenesis cluster date/times (top) and the ~~non-cyclogenesis~~ counterpart cluster date/times (middle), for forecasts that start two days prior to the cluster classifications. The bottom row shows cyclogenesis minus counterpart. Note that differences in absolute Bias and Residual are shown, so that blue (red) colours anywhere on the bottom row show where results for the cyclogenesis composite are better (worse) than for the counterpart. The two clustering regions are indicated by black borders. ~~Due to the discontinuity of date/times, diurnal-averaging prior to statistical testing and the accounting for autocorrelation are not appropriate.~~

Figure 8n indicates a significant ~~flow-dependent~~ difference in mean absolute forecast bias (of about 6 m) along the eastern coast of North America. This equates to a variance in forecast bias of $\sim 3^2 \text{ m}^2$ — suggesting that this term is as important in (the Residual term of) the day 2 extended spread-error budget for the whole of DJF 2020/21 as the explicitly represented analysis uncertainty (Fig. 6c), and would suggest an even stronger ~~over-spread~~ issue (cf. term estimates in Section 4.1, with a revised ‘reliable spread’ of $\sim 13.1^2 \text{ m}^2$). In contrast, the positive Residual term over the subtropical North Atlantic (Fig. 4.1 6e) could reflect variance in forecast bias (\sim Fig. 8n) rather than simply indicating ensemble ~~under-spread. Thinking more broadly, it under-spread.~~ It is possible that the flow-dependent variance in forecast bias might ~~also be important for have broader consequences~~ — for example in the development of “weak constraint” approaches to data assimilation, which attempt to account for model bias (Laloyaux et al., 2020). Here, in this ~~flow-dependent~~ evaluation, the ~~inter-cluster~~ variability in forecast bias is explicitly represented in Fig. 8d and Fig. 8i. Notice that the bias along the east coast of North America for the counterpart composite (Fig. 8i) appears to account for the increased errors seen in this region (compare Fig. 8f and Fig. 8a).

The overall assessment of ensemble spread is seen in the residual terms (Fig. 8e and Fig. 8j). Here it is evident ~~that almost the entire over-spread for the ECMWF ensemble that most of the over-spread~~ in the region of focus, at the head western end of the North Atlantic winter stormtrack (Fig. 6e), is associated with the cyclogenesis composite. ~~This is a key conclusion of this study.~~

~~The approach of this study was to assess reliability within a single season, because one instance of any given season is often all that is available within the operational forecast development process. One caveat to the approach taken is the lack of independent assessment; we are choosing initial conditions which we know do evolve with cyclogenesis. If anything, through “regression to the mean”, this would suggest larger errors for the cyclogenesis composite at the head of the stormtrack~~

— ~~something which is not seen~~ (cf. ~~with statistically significant residuals in Fig. 8e and statistically insignificant residuals~~ (indicated by the light blue and light grey colours) in Fig. 8j. Differences are shown in Fig. 8o. They are particularly strong and significant over Newfoundland. Downstream, differences have the opposite sign — possibly associated with differences in downstream cyclogenesis, and consistent with the increased spread noted above. Linking the day 2 stormtrack over-spread (in the region of focus) to cyclogenesis is a key conclusion of this study. It does appear, therefore, that ECMWF initial growth rates (Fig. 8a and 2, Fig. 8f)–3a) associated with cyclogenesis events are too strong. The next section explores the root-causes for this problem. Hence, we do not feel this aspect compromises the conclusions drawn here.

625 5 Sensitivity experiments — ~~including quantifying the roles to quantify sources of initial and model uncertainty in the ECMWF ensemble~~

~~The final part of this paper returns to the two case studies of cyclogenesis discussed in Sections 3.1 and ??.~~ Here, sensitivity studies are conducted to quantify the sources of uncertainty at day 2 in ECMWF's Integrated Forecasting System (IFS). The base configuration is IFS cycle 46r1, which was operational from 11 June 2019 to 20 June 2020. This includes the Ensemble of Data Assimilations (EDA), which combines observational and background information to provide the initial conditions for the ensemble forecast (ENS). Both the EDA and ENS are run at ~ 18 km resolution with 50 members. For the interested reader, the salient details of IFS cycle 46r1, along with the minor technical changes required to run the sensitivity experiments, are presented in Appendix ??.

630 In Sect. 3, the initial growth rate of uncertainty (Eq. 3) was discussed. It has subsequently been demonstrated that these growth rates are likely to be too strong in the ECMWF ensemble during cases of extratropical cyclogenesis. Here, sensitivity experiments are used to investigate why this growth rate is too strong in the ECMWF ensemble during cyclogenesis — leading to over-spread at day 2.

The configuration diagram in Fig. 9 Salient details of the ECMWF forecast system were presented in Sect. 2.1. Figure 9 shows the configuration of the sensitivity experiments. It refers to the base “operational” configuration as EDA=OP, ENS=OP. In the sensitivity experiments, this configuration is successively modified. By turning off singular vector perturbations globally (OP-SV), model uncertainty globally (OP-SV-MU) and the parametrization of deep convection in a local box (~~OP-SV-MU-DCOP-SV-MU-I~~ or increasing model horizontal grid resolution to $\sim 4 \sim 4$ km (OP-SV-MU+4km), or not assimilating observations within a given region in the EDA (OP-Obs) and again running the ENS configuration OP-SV-MU. Differences between these configurations (as indicated by the vertical allow the diagnosis of individual aspects. Vertical arrows in Fig. 9) allow the diagnosis of individual aspects indicate the sign convention of the difference to be plotted. The conclusions are not thought to be sensitive to the ordering of the various modifications. For example, it will be seen that the impacts on *total* precipitation of DCP and +4km are small, and hence these impacts should be little changed in the presence of the SPPT form of MU. However, parametrized turbulent fluxes might be weakened with +4km, and hence this impact could be a somewhat different in the presence of MU.

645 Figure 10 shows day 2 results for the standard deviation (spread) in Z_{250} from sensitivity experiments for **eyelogenesis Case-1, the cyclogenesis case** initialised at 12 UTC on 28 November 2019 (i.e., the validity time is one day later than that where the ~~growth-rate~~ growth rate fields were centred in Fig. 2 and Fig. 3a in order to see the combined effect of the

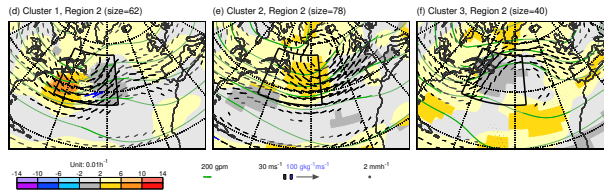


Figure 9. Configuration of IFS sensitivity experiments. These involve the Ensemble of Data Assimilations (EDA) and the Ensemble forecast (ENS). Differences between these configurations allow the diagnosis of sensitivity to individual aspects as indicated. See main text for further details.

uncertainty source and the growth rate). Grey contours show mean sea level pressure (MSL), and the black contour shows where $PV_{315} = 2P_{315} = 2$ PVU — highlighting the location of the tropopause on the 315 K isentrope) in the unperturbed EDA analysis. A parallel set of results for spread in $PV_{315} - P_{315}$ is shown in Fig. 11 (discussed later). Note that shading intervals vary over the panels shown in these two figures, so that the structures of all impacts can be seen. Mean values and

655 RMS values, integrated over the area shown, are indicated above each panel.

Figure 10a shows the OP configuration with a well-developed well-developed surface low pressure system, as discussed in relation to Fig. 1. The prominent warm conveyor belt (WCB) associated with this cyclone is seen to lead to the development of a prominent downstream upper-level ridge. The upper-level ridge and a downstream trough west of Europe. As might be expected, the maximum Z250 spread represents the temporal integral of the local tendency, and hence the effects

660 of “material” generation and advection, is located downstream of the maximum Lagrangian growth rates (cf. Fig. 3a).

The impact of the initial SV perturbations on Z250 spread (Fig. 10b) is particularly pronounced in the cyclone’s cold sector and along the downstream tropopause, along the western flanks of the two prominent troughs over the western and eastern North Atlantic, respectively. This likely indicates the potential for dynamic growth along the intense jets in these regions, qualitatively in line with the idealized studies by Hakim (2000). This SV impact might help explain the apparent slight westward shift of the centre of maximum growth in the ENS (Fig. 3a) relative to the EDA (Fig. 2). There are places where the SV impact on spread is half the total (so that the fraction of variance explained reaches 25%). The impact In contrast to the SV impact, the impact of the model uncertainty (MU) representation (Fig. 10c) is particularly pronounced in the cyclone centre and in the region of the WCB ahead of the surface low, i.e., in regions where cloud-related physical processes are particularly active. The large signal along the western flank of the ridge southwest of Greenland is consistent with the results of Joos and Forbes (2016), who found

670 a large influence of cloud microphysical processes in the WCB on the tropopause structure in this part of the downstream ridge. MU also explains up to 25% of the total variance. The remaining variance must be associated with the (deterministic) growth of initial EDA analysis uncertainty.

The Fig. 10d shows the impact of including parametrized deep convection (DC) the deep convection parametrization (DCP) in the indicated region (Fig. 10d; note the smaller contour interval). There is a reduction in the spread — particularly in the

675 WCB region — that would otherwise be created when the model attempts to resolve this convection is forced to represent this convection on its 16 km grid. This reduction in spread may go some way to explaining why Rodwell et al. (2018) identified

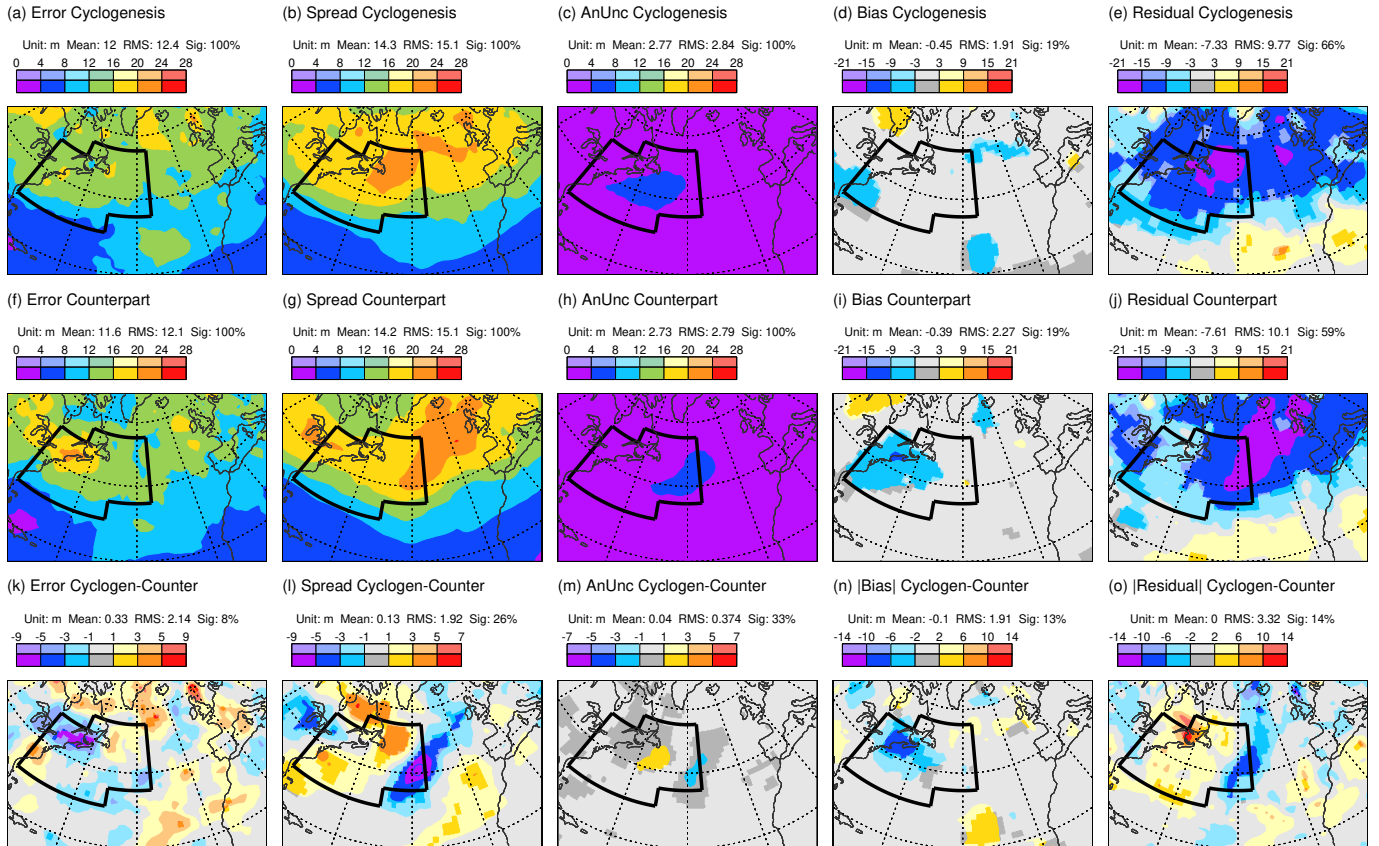


Figure 10. Sensitivity results **for cyclogenesis Case 1**, showing day-2 Z250 spread (shaded) from ECMWF ensemble forecast experiments initialised at 12 UTC on 28 November 2019. (a) Total spread for the **near-operational-near-operational** configuration OP. (b)–(f) Differences in spread between experiments which highlight the impacts of (b) including initial Singular Vector perturbations, (c) including the Model Uncertainty representation, (d) including the parametrization of Deep Convection in the indicated region $[75^{\circ}\text{W}-34^{\circ}\text{W}, 20^{\circ}\text{N}-63^{\circ}\text{N}]$, (e) an increase in model grid resolution to $\sim 4 \sim 4$ km, and (f) the assimilation of observations in the indicated region $[75^{\circ}\text{W}-47^{\circ}\text{W}, 30^{\circ}\text{N}-49^{\circ}\text{N}]$. Contours extend the shading scheme to \pm , with the same interval. In these cases, the most extreme values \pm , which are indicated at the ends of the colour bars. Also shown in each panel are the mean sea level pressure PMSL (grey contours) and $PV=2$ PVU on the 315 K isentropic (black contour) from the unperturbed EDA analysis.

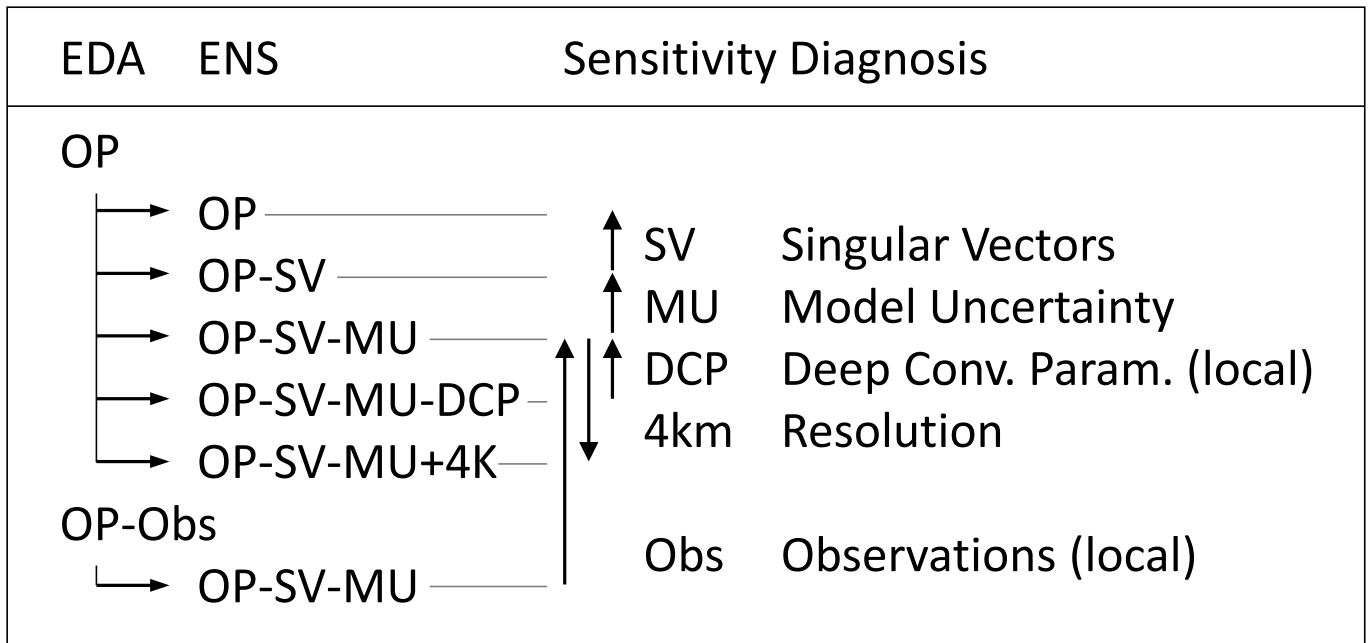


Figure 11. As Fig. 10, but shading shows the spread in PV_{315} .

~~under-spread~~ associated with mesoscale convective systems over North America. Interestingly ~~ensemble-mean~~ ensemble mean total precipitation (parametrized plus resolved) is little changed when turning off parametrized deep convection, both in location and amount (not shown).

680 The impact of increasing the model grid resolution to ~~~4~~ ~4 km is mixed. For Z_{250} spread (Fig. 10e; note the smaller contour interval), the impact is generally weak. In contrast the impact on ~~PV_{315}~~ P_{315} spread (Fig. 11e) is strong, particularly within the WCB region. ~~The smaller scales associated with PV_{315} , and its sensitivity to vertical gradients in diabatic heating in the upper troposphere might help explain this sensitivity to the increase in resolution~~ At 4 km, the model attempts to resolve more of the convection. The resolved convection can be associated with stronger updrafts, which might perturb the tropopause more vigorously, where PV gradients are particularly strong.

685 Given that model uncertainty (MU) representation is thought to partly account for the impact of ~~sub-grid-scale~~ sub-grid-scale uncertainty, perhaps the most interesting aspect here is the lack of agreement with the MU impact (cf. Fig. 11e and Fig. 11c). ~~Foreing~~ The impact on P_{315} uncertainty of allowing the model to ~~explicitly resolve this convection (even if at the wrong ~18 km scale) appears to better locate the uncertainty with that generated by the~~ ~resolve more of the convection at the 4 km km model (cf. resolution (Fig. 11e and) appears to be in closer

690 agreement with the response to turning off the deep convection parametrisation (minus Fig. 11d), when the model is forced to represent the convection on the 16 km grid. The increase in resolution also results in a small shift of ~~ensemble-mean~~ ensemble mean precipitation from parametrized to resolved, with little change in the total (not shown).

695 ~~Figure 10f shows the impact of using observations in~~ The impact of assimilating local observations is obtained using an EDA experiment (OP-Obs, see Fig. 9) where all observations were denied to the EDA in the region [75°W–47°W, 30°N–49°N] for the indicated region during the single data assimilation cycle that generated the initial conditions (as shown in Fig. 9, this impact is deduced from a data denial experiment; observations outside the indicated this region are used in both experiments). The EDA=OP and EDA=OP-Obs. It is not so easy to anticipate the impact of local observations, particularly with 4DVar, when remote observational information can propagate into the region. Results demonstrate that the assimilation of observations in this baroclinic region ~~acts to does~~ reduce initial uncertainty (not shown) ~~and to reduce day 2 spread in the developing low (Fig. 10f, and Fig. 11f).~~ This show the impact at 2 d (note the smaller contour intervals compared to those for the SV and MU impacts). There is a reduction in spread ~~is interesting because it helps quantify the role in the developing low, which suggests that the assimilation of local observations relative to that of remote observational information, which can propagate into the region within the 4DVar process, (such as cloud-affected radiances) is beneficial in this case. It is less clear whether this impact is simply a sharpening of the distribution, or whether it would also affect growth rates and reliability.~~

705 ~~Figure ?? and Fig. ?? show the corresponding results for Z250 and PV315, respectively, for the cyclogenesis Case 2. Very similar results to those above were obtained for a second set of experiments initialised at 00 UTC on 17 January 2020. Many results are similar 2020~~ — indicating that the conclusions drawn in this section are robust even with only two cases. In particular, the contributions to the total variance from SVs (Fig. ??b) and MU (Fig. ??e) and MU, with the SV impact largely ~~in the cold sector along the western flanks of the trough~~ and the MU impact in the region of the WCB. Again, the parametrization of deep convection acts to reduce spread in the WCB (Fig. ??d). ~~For PV315. For P315, the impact of increased resolution (Fig. ??e) is again more similar to the effect of turning-off convective parametrization (minus Fig. ??d) turning-off the deep convective parametrization than to that of model uncertainty (Fig. ??e). There is MU. The main difference of note is that, while there is a reduction in initial spread from the assimilation of local observations (not shown), although, it is weaker than in Case 1 the case shown above, and its impact at day 2 (Fig. ??f) and is marginal.~~

715 ~~The above results suggest that SVs, MU, and the deterministic model itself all play important roles in the early development of operational ensemble spread during cyclogenesis. (This is true globally, as can be seen in the variance spectra in Fig. ??f) is marginal. B1 in Appendix B). Since the motivation for the use of SV perturbations (Magnusson et al., 2009), and the initial reason for the development of MU representations (Buizza et al., 1999), was to increase ensemble spread, it makes sense to investigate how, jointly, these aspects might be developed to reduce the over-spread.~~

720 ~~As Fig. 10 but for Cyclogenesis Case 2, with ENS forecast experiments initialised at 00 UTC on 17 January 2020. As Fig. ??, but shading shows the spread in PV315.~~

6 Conclusions and Discussion

725 ~~The “calibration” of ensemble spread to achieve reliability in an area-mean, temporal-mean sense can only take NWP development so far. To go further, it seems important to ensure that ensembles can maintain (short-range) reliability through their development of different flow-types. This study has focused on the flow-type associated with extratropical cyclogenesis~~

730 -It has been demonstrated that the growth rate of ensemble spread in 250 hPa geopotential heights within cyclogenesis varies substantially amongst four forecast models in the “TIGGE” archive. In theory, the growth rate aims to represent (minus) the rate of change of probability density on the real world’s attractor. Studies have highlighted a range of flow features over the North American / North Atlantic / European region which can lead to a reduction in weather forecast performance (Rodwell et al., 2013; Riemer and Jones, 2014; Grams and Blumer, 2015; Lillo and Parsons, 2017; Grams et al., 2018; Baumgart and Riemer, 2019). At synoptic scales (Tribbia and Baumhefner, 2004). The Lagrangian growth rate (LGR_p , Rodwell et al., 2018) of potential vorticity, which is routinely used at ECMWF, suggests that initial upper-tropospheric uncertainty growth tends to be orchestrated around such flow features. For example, as part of extratropical cyclogenesis events, the Lagrangian growth rate in the 12 h background forecasts of the Ensemble of Data Assimilations (EDA) highlights strong uncertainty growth at the southern extent of upper-tropospheric troughs, and weaker negative growth rates (ensemble convergence) in the downstream ridge-building region (Fig. 2). This flow-dependent sensitivity to initial uncertainty in the operational forecast is the motivation for the term ‘The Cyclogenesis Butterfly’ in the title of this study.

740 The non-linear covariance terms in the generation of LGR_p (Eq. 3) are consistent with the fact that the growth rate will be sensitive to the scales of (initial) uncertainty. Since all scales contribute to EDA variance, it is unlikely that initial forecast growth rates equate directly to the intrinsic growth rates associated with the real atmosphere’s sensitivity to small scale perturbations (Durran and Gingrich, 2014). Initial growth rates associated with the ‘Cyclogenesis Butterfly’ might, however, provide support for the hypothesis of Palmer et al. (2014), that scale interactions and diabatic processes may be partially confined to intermittent synoptic flow types — as described by the Liouville equation — so there should be a “correct” solution in terms of uncertainty growth rate. While necessary approximations mean that all operational models will be compromised, it would be useful to have a framework for comparison, for deciding which model, or model update, is better able to maintain short-range reliability which could explain the longer than expected intrinsic predictability limit.

750 Following Baumgart et al. (2019) but with a focus on operational rather than intrinsic predictability, it is interesting to speculate about the processes which could give rise to strong initial growth rates LGR_p in the upper troposphere. These could include uncertainties in, for example, mid-tropospheric latent heating (e.g. Rodwell et al., 2013), deep tropospheric interactions associated with baroclinic (Hoskins et al., 1985) and associated diabatic (Ahmadi-Givi et al., 2004) processes, upper tropospheric divergence associated with dry balanced dynamics (as represented by the “Omega equation” and “Q-vectors”; Sanders and Held, 1978), nonlinear upper-tropospheric dynamics (Baumgart and Riemer, 2019), and local non-conservative processes including near-tropopause radiative forcing (Chagnon et al., 2013). Identification of the most important processes could help in the prioritisation of observational, data assimilation and modelling research. A useful goal, for example, could be to improve the analysis of the fields associated with the strongest synoptic scale initial growth rates. Here, an approach based on short-range flow-dependent evaluation of an “extended spread error equation” has been developed. It is found that the two models evaluated in this way (from ECMWF and the UK’s Met Office) are over-spread in the winter North Atlantic stormtrack (and indeed in all stormtracks). This represents a source of “untapped predictability” if it can be isolated and improved. Rather than representing a general over-spread in forecasts, it is demonstrated (for the ECMWF model over the western North Atlantic) to be associated

760 ~~with the cyclogenesis flow-type~~ it has been shown that the assimilation of local observational information can sometimes be useful (Fig. 10f, Fig. 11f).

While the EDA displays consistent flow-dependence in initial growth rates, there are differences in 12 h growth rates between ensemble systems in the TIGGE archive (Fig. 3), indicating strong sensitivity to initialisation and modelling aspects (Table 1). ECMWF generally displaying the strongest initial growth rates, and the question arises as to whether this might be ‘too strong’.

765 In an attempt to answer this question, the reliability of each ensemble system was evaluated over the December–February 2020/21 season by assessing the consistency between 2 d forecast error and spread (initially for upper-tropospheric 250 hPa geopotential heights) taking into account bias and uncertainty in the verifying analyses. Although the ECMWF ensemble displayed the smallest error, analysis uncertainty and bias (Fig. 6 columns 1,3,4) in the North Atlantic stormtrack, it was strongly over-spread (Fig. 6e). The UKMO ensemble showed the best reliability (Fig. 6 column 5). These conclusions on

770 reliability appear to generalise to other parameters (such as geopotential heights and temperatures at 500 hPa), other seasons, other stormtracks, and continue until the most recent check for the March — ~~involving an upper-level trough, and baroclinic and convective instabilities in the extra-tropics.~~ May season 2022 (not shown).

~~Case studies~~ Clustering on flow-types in the western part of the North Atlantic stormtrack (Fig. 7) demonstrated that the ECMWF over-spread in this region was associated with cyclogenesis events (Fig. 8). One consequence is that calibration

775 (possibly based on machine-learning) of ECMWF ensemble spread, without considering whether a cyclogenesis event occurred (or was likely to occur) earlier in the forecast, will likely be a blunt instrument with which to enforce reliability. In contrast, if the root cause of the over-spread can be removed, then the ensemble could gain from improved reliability *and* sharpness (the two key attributes of an ensemble system, Gneiting and Raftery, 2007).

Sensitivity studies with the ECMWF ensemble reveal the sources of uncertainty ~~during cyclogenesis~~ (Fig. 10 and Fig. 11).

780 A large part is associated with the chaotic growth of initial uncertainty within the deterministic model, ~~but singular vector~~. Results have shown that this growth rate is sensitive to the representation of deep convection in the model. However, singular vector (SV) perturbations to the initial conditions and ~~model uncertainty representations~~ the model uncertainty (MU) representation are also important. ~~Dry singular vectors, which target baroclinic instabilities (Molteni and Palmer, 1993), and which are optimised at ECMWF.~~ The dry SV perturbations applied at ECMWF, which are optimised for 2–day growth and

785 ~~which target baroclinic instabilities (Molteni and Palmer, 1993),~~ may well be implicated in the ~~over-spread.~~ ~~If so~~ over-spread. ~~If SVs are responsible,~~ then this would suggest the desirability to reduce their magnitude when other factors permit. Such a reduction would make the ensemble forecast more consistent over ~~lead-times~~ ~~lead-times~~ and permit a better use of initial ~~growth-rates~~ growth rates in the evaluation ~~of model uncertainty~~ and improvement of the model and model-uncertainty — ~~something that would be beneficial throughout the forecast range.~~ Furthermore, sensitivities to ~~switching-off~~ ~~switching-off~~ the

790 parametrization of deep convection and to increasing model resolution suggest that the model uncertainty representation ~~could~~ ~~should~~ be more strongly focused on convective instabilities (e.g., Christensen et al., 2017). ~~One might speculate whether~~ ~~It is possible that such a focus on instabilities (rather than~~ the effects of ~~moist singular vectors could be represented within the formulation of model uncertainty itself~~ ~~already-triggered instabilities)~~ might be better explored within the future ‘stochastically perturbed parameter’ (SPP) framework for model uncertainty — perturbing triggering thresholds for example.

795 *Code and data availability.* The key conclusions in this study are derived from data in the TIGGE archive, which is freely accessible. The ERA5 reanalysis data are also freely available. Other data and diagnostic code are available from the authors upon request.

~~code available~~

Video supplement. Growth rate animations are available as supplementary material.

Appendix A: ~~Derivation of local growth-rate equation for isentropic PV~~ Estimating the other terms in the residual

800 If P_i, \mathbf{v}_i are the isentropic potential vorticity and horizontal wind vector for ensemble member i ($= 1, \dots, m$), respectively, then $\partial P_i / \partial t + \mathbf{v}_i \cdot \nabla_\theta P_i = NC_i$, where t is time, ∇_θ is the gradient operator on the isentropic surface θ , and NC_i represents the effects of “non-conservative” diabatic and frictional processes. Using an overline to denote a mean $\bar{X} = m^{-1} \sum_i X_i$, and a prime to denote deviations from the mean $X'_i = X_i - \bar{X}$, then the variance of the P_i can be written as $\hat{\sigma} = \overline{P'^2}$, and the local growth-rate of the standard deviation written as-

805

It is useful to write $b_j = \mu_{\tilde{A}_j} - \mu_{A_j}$ (= minus term 6 in Eq. (4)) for the bias in the verifying analysis distribution associated with a given realisation of the truth, and subsequent assimilation of observations. Then, from Eq. (5), the expected bias in the verifying analysis is given by $\mathbb{E}_j[b_j] = \beta_{\tilde{A}_j}$.

Appendix B: ~~Further details on the growth-rate plots~~

810 Figure 2 and Fig. ??, and animations 1 and 2 in the supplementary material show, for the two cyclogenesis cases, the growth-rate With reference to the numbered terms in Eq. (??; left-hand-side) in the ensemble standard deviation of potential vorticity on the 315 K isentrope $\hat{\sigma}_{PV315}$ following the ensemble mean horizontal flow $\bar{\mathbf{v}}_{315}$. This 4), one potential cross term contained in \mathcal{E}_j of Eq. (6) is $2\mathbb{E}_j[1 \cdot 6] = 2\sigma_{T_j b_j}$. This might be non-zero if the analysis bias is dependent on the true state (the covariance $\sigma_{T_j b_j}$, when divided by $\sigma_{T_j}^2 = \sigma_{\tilde{F}_j}^2$, measures the linear dependence of the analysis bias on the

815 truth). In the ECMWF EDA, each analysis member is an innovation of that member’s background forecast, and this lack of independence might imply that the cross-term $2\mathbb{E}_j[2 \cdot 4] = -\frac{2}{m} \sigma_{\tilde{F}_j} \tilde{\alpha}_j$ is derived from background (first-guess) forecasts within the ECMWF operational EDA (see Appendix ??), initialised at 06 and 18 UTC, and for hourly lead-times 0–12 h. Fields of PV_{315} and zonal and meridional winds at 315 K (u_{315} and v_{315}) are interpolated to an “N32” reduced-Gaussian grid (with 32 latitudes between the pole and equator). The spatial derivatives within the advection non-zero, particularly at very

820 short leadtimes and for small ensemble size m . All other cross-terms are likely to have zero expectation with the exception of $2\mathbb{E}_j[5 \cdot 6] = -2\beta_{\tilde{F}_j} \beta_{\tilde{A}_j}$, which is explicitly represented in the $\beta_{\tilde{A}_j}^2$ term in Eq. (??) are calculated using spectral transforms to and from a “T42” spherical harmonic representation (total wavenumbers ≤ 42). Note that N32 is sufficient to avoid

aliasing of higher harmonics of the quadratic advection term into the T42 representation. To focus on synoptic spatial scales, $\widehat{\sigma}_{PV315}$ and the growth rate of $\widehat{\sigma}_{PV315}$ are then spatially smoothed by multiplying spectral coefficients (with total wavenumber $n > n_s = 21$) by $\{n_s(n_s + 1)\}/\{n(n + 1)\}$. For the lower-tropospheric fields shown, zonal and meridional winds and specific humidities at 850 hPa ($u315, v315, q850$) and surface pressure p_* , all from the background forecasts of the control EDA member, are first interpolated to an ‘‘O32’’ octahedral reduced-Gaussian grid (with 32 latitudes between the pole and equator). Values are set to ‘‘missing’’ where the 850 hPa surface is below the land surface (where $p_* < 850$ hPa) and the moisture flux is calculated as $q850\sqrt{u850^2 + v850^2}$. The ensemble-mean total precipitation rate is used to indicate where precipitation is likely to occur. This is obtained on a higher resolution ‘‘O80’’ octahedral grid to give a good symbolic representation (stippling) of rainfall. To focus on synoptic timescales, a 1-day running mean is applied to all fields before plotting. Note that animation 3 in the supplementary material shows the animation for the entire DJF 2019/20 season. 6). Finally note that $\mathbb{E}_j[\mathbf{6}^2] = \mathbb{V}_j[\mathbf{6}] + \beta_{Aj}^2$ and so \mathcal{E}_j should also include $\mathbb{V}_j[\mathbf{6}] \equiv \sigma_{bj}^2$, the (expected) variance of the analysis bias. Hence

Figure 3 and Fig. ?? and animations 4 and 5 in the supplementary material show, for the two cyclogenesis cases, the growth-rate in the ensemble standard deviation of geopotential height at 250

$$\mathcal{E}_j \approx 2\sigma_{T_j b_j} - \frac{2}{m}\sigma_{\bar{F}_j \bar{A}_j} + \sigma_{b_j}^2 \quad . \quad (\text{A } 1)$$

The expected residual in Eq. (8) can then be written as

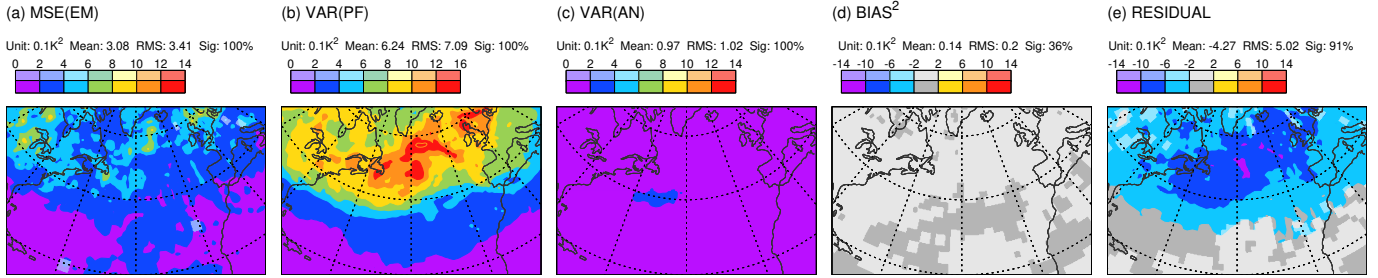
$$\mathbb{E}[R] = \mathbb{E}\left[(\sigma_F^2 - \sigma_{\bar{F}}^2) + (\sigma_A^2 - \sigma_{\bar{A}}^2)\right] + \mathbb{E}\left[2\sigma_{Tb} - \frac{2}{m}\sigma_{\bar{F}\bar{A}} + \sigma_b^2\right] + \sigma_\beta^2 \quad , \quad (\text{A } 2)$$

As noted in the main text, all terms that involve variations in bias have been moved into the residual. These terms are difficult to estimate, but an attempt is made here for day-2 forecasts of temperatures at 500 hPa $\widehat{\sigma}_{Z250}$ following the ensemble-mean horizontal flow \bar{v}_{250} for the four chosen TIGGE models. Animation 6 in the supplementary material shows the entire DJF 2019/20 during the December–February (DJF) season. These are derived from ensemble data obtained from the TIGGE archive for forecasts initialised at 00 and 12 UTC, and for lead times 0, 6, 12 h. All other aspects are the same as for the plots of the $\widehat{\sigma}_{PV315}$ growth-rate with the exception that the plotted Z250 field is not spatially smoothed (it is considered already a synoptic-scale field). For reference, Fig. A1 shows the corresponding (non-rooted version of) the extended spread-error equation. Consistent with the Z500 result in the main text, this also highlights a potential over-spread in the stormtrack. The following list outlines the approach taken here to estimate the right-most four terms in Eq. (A 2).

Appendix B: Derivation of the ‘‘extended spread-error’’ equation

where the last line is just a convenient re-arrangement of the terms on the second line.

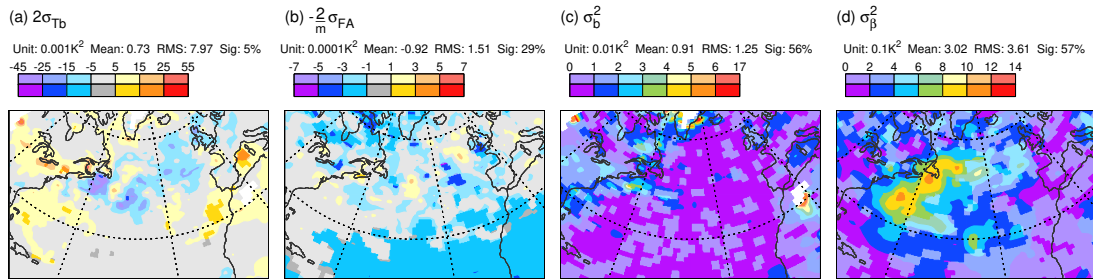
1. $2\mathbb{E}[\sigma_{Tb}]$ in Eq. (A 2) is tricky to estimate as it requires the state-dependent estimation of analysis bias. One approach is to utilise inter-annual variability over the n_u (4) would be difficult to quantify in the operational forecast system



With reference to the schematic shown in Fig. 5, consider initially a single ensemble forecast, and thus consider an initial time t_j for some fixed value of j . Next consider a perfectly reliable forecast/analysis system. As discussed in section ??, the verifying truth T_j should be statistically indistinguishable from any random sampling of the forecast distribution F_j . This distribution need not be Gaussian or even uni-modal, but let it have mean μ_{F_j} and variance $\sigma_{F_j}^2$. The verifying analysis distribution A_j is constructed using observations of the truth (amongst other things), so that its mean and variance will be the conditional random variables $\mu_{A_j|T_j}$ and $\sigma_{A_j|T_j}^2$. Again, for a reliable analysis distribution, the T_j should be statistically indistinguishable from any random sampling of A_j . (Because of the conditionality above, it is actually uncertainties in the analysis distribution which can enable this). Now consider a realistic forecast/analysis system which need not be reliable. Let the “underlying” forecast distribution \tilde{F}_j have mean $\mu_{\tilde{F}_j}$ and variance $\sigma_{\tilde{F}_j}^2$, and the underlying verifying analysis distribution \tilde{A}_j have mean $\mu_{\tilde{A}_j}$ and variance $\sigma_{\tilde{A}_j}^2$. Finally, let the estimators of these quantities based on the real ensemble (finite samplings of \tilde{F}_j and \tilde{A}_j) be $\hat{\mu}_{\tilde{F}_j}$, $\hat{\sigma}_{\tilde{F}_j}^2$, $\hat{\mu}_{\tilde{A}_j}$ and $\hat{\sigma}_{\tilde{A}_j}^2$. The departure of the ensemble-mean forecast $\hat{\mu}_{\tilde{F}_j}$ from the ensemble-mean analysis $\hat{\mu}_{\tilde{A}_j}$ can then be written (by following the other lines in Fig. 5) as:-

Figure A1. Extended spread-error budget (squared terms) for DJF 2020/21 for temperature at 500 hPa on day 2 from ECMWF ensemble forecasts. Statistically significant values are shown with more saturated colours. Area means (for the area displayed) are indicated at the top of each panel (e.g. “Sig: 85%” means that 85% of the area is significant at the 5% significance level).

$$\begin{aligned}
 d_j &= (\hat{\mu}_{\tilde{F}_j} - \hat{\mu}_{\tilde{A}_j}) \\
 &= (\hat{\mu}_{\tilde{F}_j} - \mu_{\tilde{F}_j}) + (\mu_{\tilde{F}_j} - \mu_{F_j}) + (\mu_{F_j} - T_j) + (T_j - \mu_{A_j}) + (\mu_{A_j} - \mu_{\tilde{A}_j}) + (\mu_{\tilde{A}_j} - \hat{\mu}_{\tilde{A}_j}) \\
 &= \underbrace{(\mu_{F_j} - T_j)}_1 + \underbrace{(\hat{\mu}_{\tilde{F}_j} - \mu_{\tilde{F}_j})}_2 + \underbrace{(T_j - \mu_{A_j})}_3 + \underbrace{(\mu_{\tilde{A}_j} - \hat{\mu}_{\tilde{A}_j})}_4 + \underbrace{(\mu_{\tilde{F}_j} - \mu_{F_j})}_5 + \underbrace{(\mu_{A_j} - \mu_{\tilde{A}_j})}_6,
 \end{aligned}$$



The terms 1–6 in

Figure A2. Estimates of the magnitudes of the ‘other terms’ included in the Residual for temperatures at 500 hPa during the period DJF 2020/21. (a) Covariance of the analysis bias with the atmospheric state ($\times 2$). (b) Covariance of the ensemble-mean day+2 forecast and ensemble-mean analysis ($\times -2$). (c) Variance of the analysis bias. (d) Variance of the day+2 forecast bias (relative to analysis). Statistically significant values are shown with more saturated colours. Area means (for the area displayed) are indicated at the top of each panel (e.g. “Sig: 29%” means that 29% of the area is significant at the 5% significance level). Please see main text for further details.

because they require knowledge of the truth and ≈ 10) years 2012–2021, and to regress the DJF-mean analysis bias (relative to a set of observations) against the DJF-mean observations themselves. The so-called ‘analysis departure’ is the observation minus the analysis-equivalent of the observation (after applying the relevant ‘observation operator’). Assuming that the moments of the underlying distributions (only $d_j, \hat{\mu}_{F_j}$ analysis bias (here for temperatures at 500 hPa, T500) closely matches minus the mean analysis departure from the observations (here “AMSUA” channel 5 satellite brightness temperatures which measure “mid-tropospheric” temperatures with a maximum weighting at ~ 500 hPa - these observations have had ‘variational bias correction’, VarBC, applied), we can make the estimate

$$2\mathbb{E}[\sigma_{Tb}] \approx -\frac{2m}{m-1} \frac{\hat{\sigma}_{o(o-a)}}{\hat{\sigma}_o^2} \hat{\sigma}_F^2, \quad (\text{A } 1)$$

where o refers to the seasonal-means of the observations, and $\hat{\mu}_{A_j}$ are quantifiable). Nevertheless, we can discuss their expected values. Define $\mathbb{E}_j[\cdot]$ to be the expectation for a given j . Since j is fixed, so are the distributions F_j - a refers to the seasonal-means of the analyses. Notice that the bias variations are scaled to reflect the synoptic variations in truth during DJF 2021. Figure A2(a) shows that, over the North Atlantic, this estimated covariance is $\sim 0.025 \text{ K}^2$. This is generally smaller in magnitude than the analysis variance shown in Fig. A1 (top, third from left, $\sim 0.2 \text{ K}^2$) and \hat{F}_j ; the expectation is over all samplings \hat{F}_j of \tilde{F}_j , all potential T_j and corresponding analysis distributions A_j and \tilde{A}_j , and all samplings \hat{A}_j of \tilde{A}_j . Taking the expectation of the last line more clearly smaller than the current residual (top, far right, $\sim 0.6 \text{ K}^2$). Although the brightness observations have themselves had a bias correction applied, there is a potential that this is not perfect, and that remaining variations in observational bias might affect our analysis bias estimation here. ‘Radio-occultation’ observations, which are beginning to become more numerous, may offer the prospect of a more pure estimate of analysis bias in the future.

2. σ_b^2 in Eq. (4) can also be estimated by utilising inter-annual variability of seasonal-means:

$$\mathbb{E}_j[d_j] = \mathbb{E}_j \left[\sigma_b^2 \right] = \mathbb{E}_j(\mu_{\tilde{F}j} - \mu_{Fj}) - (\mu_{\tilde{A}j} - \mu_{Aj}) \equiv \beta_{\tilde{F}j} - \beta_{\tilde{A}j} \equiv \beta_j \approx \frac{n' n_y}{n_y - 1} \hat{\sigma}_{(o-a)}^2 \quad , \quad (\text{A } 2)$$

since terms 1–4 in Eq. (4) have zero expectation. Hence $\mathbb{E}_j[d_j] = \beta_j$: the expected bias of the unreliable forecast $\beta_{\tilde{F}j}$ minus the expected bias of the unreliable analysis $\beta_{\tilde{A}j}$. As lead-time increases, one might expect that the forecast bias will become the dominant component of β_j where the multiplier n' is the number of synoptic degrees of freedom in a season (here $n' = 30$ assuming a 3-day synoptic decorrelation timescale). Figure A2(c) shows that this term is also of order $\sim 0.02 \text{ K}^2$ in the North Atlantic region, so again smaller than the analysis variance and residual terms.

The “extended spread-error equation” is based on the expected square of Eq. (4). This involves squared terms, such as $\mathbb{E}_j[1-1]$, and cross-terms, such as $2\mathbb{E}_j[1-6]$. In general the squared terms might be thought to dominate, leading to (in the same order as the last line in

3. σ_β^2 in Eq. (4) can be estimated by trying a similar approach:

$$\mathbb{E} \left[\sigma_\beta^2 \right] \approx \frac{n' n_y}{n_y - 1} \hat{\sigma}_{(f-a)}^2 \quad , \quad (\text{A } 3)$$

The term in parentheses $\{ \}$ comprises the “variance deficit” (which compares the reliable and unreliable variances of the ensemble forecast and analysis) and \mathcal{E}_j , which collects any potentially non-zero cross-terms and the (expected) variance in analysis bias (see later for further discussion).

From Eq. (6), the expected squared departure (over an infinite set of initial forecast times t_j) can then be written as

$$\mathbb{E}[d^2] = \frac{m+1}{m} \mathbb{E}[\sigma_{\tilde{F}}^2 + \sigma_{\tilde{A}}^2] + \mathbb{E}[\beta]^2 + \mathbb{E}[R] \quad ,$$

with expected “residual”,

$$\mathbb{E}[R] = \mathbb{E} \left[(\sigma_{\tilde{F}}^2 - \sigma_{\tilde{F}}^2) + (\sigma_{\tilde{A}}^2 - \sigma_{\tilde{A}}^2) \right] + \mathbb{E}[\mathcal{E}] + \sigma_\beta^2 \quad ,$$

where $\sigma_\beta^2 = \mathbb{V}[\beta]$ accounts for the explicit replacement of $\mathbb{E}[\beta^2]$ with $\mathbb{E}[\beta]^2$ in Eq. (7). It can be seen that all terms that involve variations in bias have been moved into the residual. f refers to the day+2 seasonal-means of the (deterministic HRES) forecasts. Figure A2(d) shows that this term is of order $\sim 1 \text{ K}^2$ over the western North Atlantic region. This

895 may be an over-estimate since reducing predictive skill with lead-time means that $(f - a)$ begins to reflect (minus) the observed anomaly from climate, and thus becomes less useful at indicating forecast bias as the forecast lead-time increases (e.g. by day+10). Nevertheless, variations in forecast bias may well be non-negligible, and would imply here that the over-spread is even larger over the western North Atlantic. Flow-dependent evaluation of the extended spread-error budget, discussed later, represents a means of avoiding issues with forecast bias variations.

For an unbiased estimator of

900 4. $-\frac{2}{m}\sigma_{\tilde{F}\tilde{A}}$ in Eq. (7), we note that $(\mathbb{E}[d^2] - \mathbb{E}[\beta]^2) = (\mathbb{E}[d^2] - \mathbb{E}[d]^2) = \mathbb{V}[d]$ which has unbiased estimator $\frac{n}{n-1}(\bar{d}^2 - \bar{d}^2)$, and obtain the extended spread-error equation: A 2) does not involve bias and can be estimated in-sample as

$$\frac{n}{n-1}\bar{d}^2 = \frac{m+1}{m-1}(\hat{\sigma}_{\tilde{F}}^2 + \hat{\sigma}_{\tilde{A}}^2) + \frac{n}{n-1}\bar{d}^2 + \bar{R} \quad ,$$

where \bar{R} can be written as the mean of the residuals R_j :

$$R_j \equiv \frac{n}{n-1}d_j^2 \mathbb{E}\left[-\frac{2}{m}\sigma_{\tilde{F}\tilde{A}}\right] \approx -\frac{m+1}{m-1}\frac{2}{\tilde{F}_j} + \frac{2}{m-1}\frac{2}{\tilde{A}_j}\overline{\hat{\sigma}_{\tilde{F}\tilde{A}}} \quad (A 4)$$

905 which close the budget for each initial time (for given, constant \bar{d}). The extent to which \bar{R} is a good estimate for the expected “variance deficit” in Eq. (8) will depend on the magnitude of The scale to the other terms $\mathbb{E}[\mathcal{E}] + \sigma_{\beta}^2$ in Eq. (8). The only potentially non-zero terms in $\mathbb{E}[\mathcal{E}]$ appear to be $2\mathbb{E}_j[1-6]$ (if the analysis bias is dependent on the true state), $2\mathbb{E}_j[2-4]$ (at short lead-times and for small ensemble sizes if the analysis is dependent on background forecasts) and the expected variance of the analysis bias (a component of $\mathbb{E}_j[6-6]$). These terms are difficult to quantify but estimation suggests that they are likely to be negligible (the estimation was based on 10 DJF seasons, a 50-member ensemble size, day-2 temperatures at 500 hPa, and analysis departures from “AMSUA” satellite channel 5 brightness temperatures). Thus the only additional term that may need accounting for is the colour bar in Fig. A2(b) shows that this term is several orders of magnitude smaller than the analysis variance and residual terms.

915 Considering all these terms, it appears that the residual in the day+2 T500 budget largely represents the ensemble variance deficit and, possibly, the variance in forecast bias σ_{β}^2 - which is appreciable in the cyclogenesis region off the east coast of North America. Ideally such an analysis would be made for all variables for which the budget is calculated. However, σ_{β}^2 . In the flow-dependent evaluation discussed here, this is (at least partially) accounted for explicitly (and is non-negligible) difficult for many variables and here we will assume that the T500 analysis carries-over to other variables of the large-scale flow.

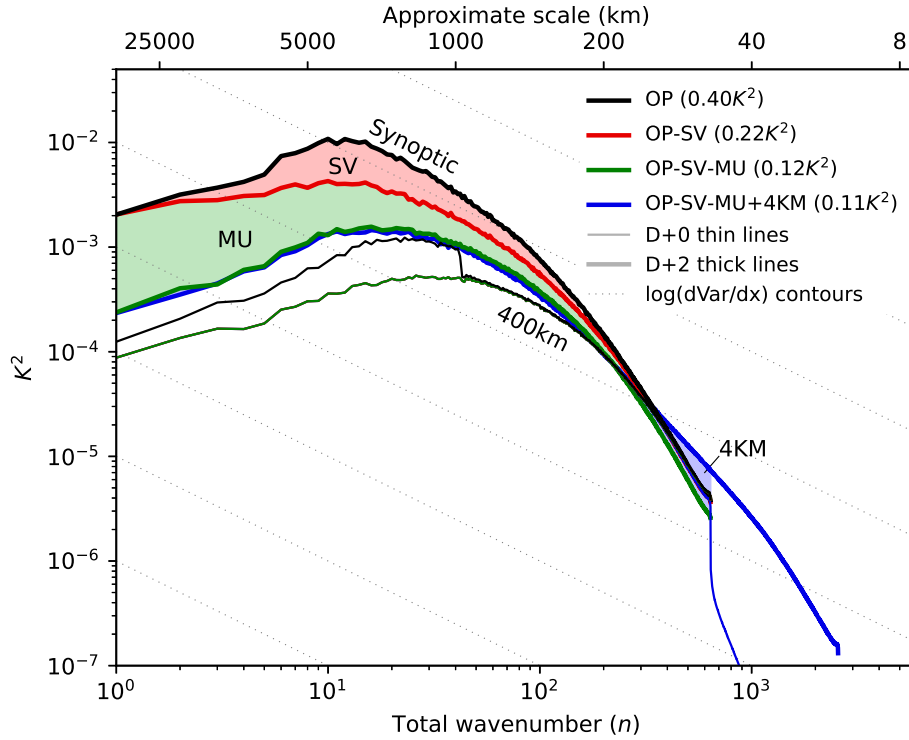
Appendix B: Global plots of Variance spectra for the extended spread-error equationsensitivity experiments

Figure ?? and Fig. ?? show global plots of

920 Figure B1 shows the variance spectra of global spherical harmonics against total wavenumber for the experiments discussed in Sect. 5. The approximate scale is indicated on the top x-axis. Initial uncertainty from the EDA (Fig. B1, thin green curve) occurs at all scales, with the largest variance contributions at scales ~ 400 km. The thin black curve shows the initial spectrum after addition of the singular vector (SV) perturbations (at scales ≥ 1000 km). The contributions to day 2 variance associated with SV perturbations and model uncertainty (MU) representation are indicated by the red and green shaded regions, 925 respectively. SVs contribute strongly at synoptic scales while MU contributes at synoptic and planetary scales. The thick green curve indicates the impact of pure chaotic growth of EDA uncertainty without SVs or MU in the forecast). Notice that the day 2 and EDA variance spectra coincide at scales smaller than ~ 100 km — indicating that the EDA variance is already saturated at these scales. The thick blue curve shows the day 2 spectrum when the gridpoint resolution of the forecast model is increased to ~ 4 km. The spectrum is seen to ‘shallow’ even at scales already represented by the original ~ 16 km model (as indicated by the 930 blue shaded region). A similar plot based on the extended spread error equation, applied to geopotential height at 500 same set of experiments for the second initial date (00 hPa at day-2 in their non-rooted form, for DJF UTC on 17 January 2020/21 and JJA 2021 seasons, respectively. ECMWF displays smaller root-mean-square errors of the ensemble-mean than UKMO, and smaller analysis uncertainty. In all winter stormtrack regions, ECMWF shows larger spread (and over-spread) than UKMO. In polar regions, UKMO shows larger spread (and over-spread) than ECMWF.) is almost indistinguishable from Fig. B1. 935 As Fig. ??, but for June — August 2020 Eq. (9).

Appendix C: Salient aspects of ECMWF’s Integrated Forecasting System

The sensitivity studies are based on cycle 46r1 of the IFS. This cycle was operational from 11 June 2019 to 20 June 2020. The underlying model uses spherical harmonics to compute much of the dynamics, with physical parametrizations computed in grid-point space. Of particular interest here is the parametrization of convection, which was originally based on Tiedtke (1989), 940 but includes revisions to entrainment and coupling with the large scale (Bechtold et al., 2008; Hirons et al., 2013), and improvements in the diurnal cycle of convection through use of a modified convective available potential energy (CAPE) closure (Bechtold et al., 2014). This model is used within the EDA (Isaksen et al., 2010) and the ENS (Palmer et al., 1992; Molteni et al., 1996). The 50-member EDA has horizontal grid resolution ~ 18 km (the model’s spectral resolution is T639 and a cubic “octahedral” grid is used so that 4 grid-points represent the smallest waves — the resolution is thus summarised as TCo639) with 137 levels in the 945 vertical (L137) and a 12 min timestep. 4D Variational data assimilation (4DVar, Rabier et al., 2000) is used to extract the information content from many millions of conventional and satellite observations during each 12 h analysis cycle. After initial screening, observations are corrected using Variational Bias Correction (VarBC, Dec, 2004) and randomly perturbed in each EDA member to simulate observation uncertainty (Isaksen et al., 2010). Background uncertainty is dynamically based on the background spread over recent cycles, with a climatological component for stability (Bonavita et al., 2016). The EDA is used 950 to initiate a 50-member ENS, with resolution TCo639, L91 and a 12 min timestep. Initial conditions are re-centred on a more recent (“Early Delivery”) unperturbed high-resolution (HRES) analysis. SV perturbations are added to the initial conditions



As Fig. 6, but for geopotential height at 500 hPa and showing global maps of the (non-rooted) terms in the extended spread-error budget Eq. (9). Simple differences are shown in the bottom panels.

Figure B1. Spectra of ensemble variance for the indicated experiments, summarised in Fig. 9. Spectra show the variance of the ensemble filtered on total wavenumber n for global spherical harmonics. The approximate scale of each harmonic is indicated on the top x-axis (this relates to a half wavelength assuming equal zonal and meridional wavenumbers). Thin lines show initial time and thick lines show day 2. The red, green and blue shaded regions indicate the impacts at day 2 of including initial singular vector (SV) perturbations, model uncertainty (MU) representation and increasing the gridpoint resolution of the forecast model to ~ 4 km. Diagonal dotted lines are contours of variance contribution per linear unit length on the x-axis, with contour value indicated where they intersect the y-axis. Total variance for each experiment is indicated in parenthesis in the key.

as a pragmatic means of boosting ENS spread over the first 2 days (Molteni and Palmer, 1993; Leutbecher and Lang, 2014). A model uncertainty (MU) parametrization, which partly aims to represent the up-scale response sub-grid-scale uncertainty, is important for the general growth of ENS spread into the medium-range (e. g., to day 10). This MU representation is currently
955 based on “Stochastic Perturbation to Physical Tendencies” (SPPT, Buizza et al., 1999), and is applied in the non-linear outer-loops of the EDA as well as in the ENS.

In the experiments here, VarBC and SPPT are “warm-started” from the operational assimilation, ENS initial condition re-centring is not done, and SV perturbation scaling is based on the current EDA cycle rather than the previous cycle. In the
~4 km ENS resolution experiment, the model is run in “single precision” (Váña et al., 2017; Lang et al., 2021) with resolution
960 TCo2559-L91 and a 4 min timestep.

Author contributions. This study arose from close collaboration between the authors during HW’s period as an ECMWF Fellow, and from ideas generated in the Warm Conveyor Belt workshop, which they co-organised in 2020. The mathematical content and much of the diagnostic work for this study was completed by MJR, with HW providing important guidance throughout.

Competing interests. The authors have no competing interests in this study

965 *Acknowledgements.* For the sensitivity experiments, ~~considerable help came from~~ the authors would like to thank Peter Bechtold, Andrew Dawson, Richard Forbes, Alan Geer, Elias Hólm, Bruce Ingleby, Simon Lang, Inna Polichtchouk, and Gabor Radnoti for their considerable. The authors would also like to thank Katharina Heitmann (ETH Zurich) for preparing Fig. 1 and Jonathan Day, Rebecca Emerton, David Lavers, Linus Magnusson, Florian Pappenberger, and David Richardson for useful discussions about this work. Finally, the authors would like to express their great appreciation to the two reviewers for their time and inciteful remarks, which have led to improvements in this
970 manuscript.

References

- Ahmadi-Givi, F., Graig, G. C., and Plant, R. S.: The dynamics of a midlatitude cyclone with very strong latent-heat release, *Quart. J. Roy. Meteor. Soc.*, 130, 295–323, <https://doi.org/10.1256/qj.02.226>, 2004.
- 975 Baumgart, M. and Riemer, M.: Processes governing the amplification of ensemble spread in a medium-range forecast with large forecast uncertainty, *Quart. J. Roy. Meteor. Soc.*, 145, 3252–3270, <https://doi.org/https://doi.org/10.1002/qj.3617>, 2019.
- Baumgart, M., Ghinassi, P., Wirth, V., Selz, T., Craig, G. C., and Riemer, M.: Quantitative View on the Processes Governing the Upscale Error Growth up to the Planetary Scale Using a Stochastic Convection Scheme, *Mon. Wea. Rev.*, 147, 1713–1731, <https://doi.org/10.1175/MWR-D-18-0292.1>, 2019.
- 980 Bechtold, P., Köhler, M., Jung, T., Doblas-Reyes, F., Leutbecher, M., Rodwell, M. J., Vitart, F., and Balsamo, G.: Advances in simulating atmospheric variability with the ECMWF model: From synoptic to decadal time-scales, *Quart. J. Roy. Meteor. Soc.*, 134, 1337–1351, 2008.
- Bechtold, P., Semane, N., Lopez, P., Chaboureaud, J., Beljaars, A., and Bormann, N.: Representing Equilibrium and Nonequilibrium Convection in Large-Scale Models, *J. Atmos. Sci.*, 71, 734 – 753, <https://doi.org/10.1175/JAS-D-13-0163.1>, 2014.
- 985 Bishop, C. H., Etherton, B. J., and Majumdar, S. J.: Adaptive Sampling with the Ensemble Transform Kalman Filter. Part I: Theoretical Aspects, *Mon. Wea. Rev.*, 129, 420 – 436, [https://doi.org/10.1175/1520-0493\(2001\)129<0420:ASWTET>2.0.CO;2](https://doi.org/10.1175/1520-0493(2001)129<0420:ASWTET>2.0.CO;2), 2001.
- Bonavita, M., Hólm, E., Isaksen, L., and Fisher, M.: The evolution of the ECMWF hybrid data assimilation system, *Quart. J. Roy. Meteor. Soc.*, 142, 287–303, <https://doi.org/10.1002/qj.2652>, 2016.
- Buizza, R., Miller, M., and Palmer, T. N.: Stochastic representation of model uncertainties in the ECWMF Ensemble Prediction System, *Quart. J. Roy. Meteor. Soc.*, 125, 2887–2908, <https://doi.org/10.1002/qj.49712556006>, 1999.
- 990 Chagnon, J. M., Gray, S. L., and Methven, J.: Diabatic processes modifying potential vorticity in a North Atlantic cyclone, *Quart. J. Roy. Meteor. Soc.*, 139, 1270–1282, <https://doi.org/https://doi.org/10.1002/qj.2037>, 2013.
- Christensen, H. M.: Constraining stochastic parametrisation schemes using high-resolution simulations, *Quart. J. Roy. Meteor. Soc.*, 146, 938–962, <https://doi.org/https://doi.org/10.1002/qj.3717>, 2020.
- 995 Christensen, H. M., Lock, S.-J., Moroz, I. M., and Palmer, T. N.: Introducing independent patterns into the Stochastically Perturbed Parametrization Tendencies (SPPT) scheme, *Quart. J. Roy. Meteor. Soc.*, pp. n/a–n/a, <https://doi.org/10.1002/qj.3075>, 2017.
- Dee, D. P.: Variational bias correction of radiance data in the ECMWF system., in: *ECMWF Workshop on Assimilation of High Spectral Resolution Sounders in NWP*, pp. 97–112, ECMWF, Shinfield Park, Reading, Berkshire, RG2 9AX, UK, 2004.
- Durrán, D. R. and Gingrich, M.: Atmospheric Predictability: Why Butterflies Are Not of Practical Importance, *J. Atmos. Sci.*, 71, 2476–2488, <https://doi.org/10.1175/JAS-D-14-0007.1>, 2014.
- 1000 Ehrendorfer, M.: The Liouville Equation and Its Potential Usefulness for the Prediction of Forecast Skill. Part I: Theory, *Mon. Wea. Rev.*, 122, 703 – 713, [https://doi.org/10.1175/1520-0493\(1994\)122<0703:TLEAIP>2.0.CO;2](https://doi.org/10.1175/1520-0493(1994)122<0703:TLEAIP>2.0.CO;2), 1994.
- Evensen, G.: Sequential data assimilation with a nonlinear quasi-geostrophic model using Monte Carlo methods to forecast error statistics, *J. Geophys. Res.*, 99, 10 143–10 162, <https://doi.org/10.1029/94JC00572>, 1994.
- 1005 Geer, A. J., Lonitz, K., Weston, P., Kazumori, M., Okamoto, K., Zhu, Y., Liu, E. H., Collard, A., Bell, W., Migliorini, S., Chambon, P., Fourrié, N., Kim, M.-J., Köpken-Watts, C., and Schraff, C.: All-sky satellite data assimilation at operational weather forecasting centres, *Quart. J. Roy. Meteor. Soc.*, 144, 1191–1217, <https://doi.org/https://doi.org/10.1002/qj.3202>, 2018.

- Gneiting, T. and Raftery, A. E.: Strictly Proper Scoring Rules, Prediction, and Estimation, *J. Am. Statist. Assoc.*, 102, 359–378, <https://doi.org/10.1198/016214506000001437>, 2007.
- Grams, C. M. and Blumer, S. R.: European high-impact weather caused by the downstream response to the extratropical transition of North Atlantic Hurricane Katia (2011), *Geophys. Res. Lett.*, 42, 8738–8748, <https://doi.org/https://doi.org/10.1002/2015GL066253>, 2015.
- Grams, C. M., Magnusson, L., and Madonna, E.: An atmospheric dynamics perspective on the amplification and propagation of forecast error in numerical weather prediction models: A case study, *Quart. J. Roy. Meteor. Soc.*, 144, 2577–2591, <https://doi.org/https://doi.org/10.1002/qj.3353>, 2018.
- Hakim, G. J.: Role of Nonmodal Growth and Nonlinearity in Cyclogenesis Initial-Value Problems, *J. Atmos. Sci.*, 57, 2951–2967, [https://doi.org/10.1175/1520-0469\(2000\)057<2951:RONGAN>2.0.CO;2](https://doi.org/10.1175/1520-0469(2000)057<2951:RONGAN>2.0.CO;2), 2000.
- Hamill, T. M.: Interpretation of Rank Histograms for Verifying Ensemble Forecasts, *Mon. Wea. Rev.*, 129, 550–560, [https://doi.org/10.1175/1520-0493\(2001\)129<0550:IORHFV>2.0.CO;2](https://doi.org/10.1175/1520-0493(2001)129<0550:IORHFV>2.0.CO;2), 2001.
- Hartigan, J. A. and Wong, M. A.: Algorithm AS136: A K-means clustering algorithm, *J. R. Stat. Soc., C: Appl. Stat.*, 28, 100–108, 1979.
- Hersbach, H., Bell, B., Berrisford, P., Hirahara, S., Horányi, A., Muñoz Sabater, J., Nicolas, J., Peubey, C., Radu, R., Schepers, D., Simmons, A., Soci, C., Abdalla, S., Abellan, X., Balsamo, G., Bechtold, P., Biavati, G., Bidlot, J., Bonavita, M., De Chiara, G., Dahlgren, P., Dee, D., Diamantakis, M., Dragani, R., Flemming, J., Forbes, R., Fuentes, M., Geer, A., Haimberger, L., Healy, S., Hogan, R. J., Hólm, E., Janisková, M., Keeley, S., Laloyaux, P., Lopez, P., Lupu, C., Radnoti, G., de Rosnay, P., Rozum, I., Vamborg, F., Villaume, S., and Thépaut, J.-N.: The ERA5 global reanalysis, *Quart. J. Roy. Meteor. Soc.*, 146, 1999–2049, <https://doi.org/https://doi.org/10.1002/qj.3803>, 2020.
- Hirons, L. C., Inness, P., Vitart, F., and Bechtold, P.: Understanding advances in the simulation of intraseasonal variability in the ECMWF model. Part I: The representation of the MJO, *Quart. J. Roy. Meteor. Soc.*, 139, 1417–1426, <https://doi.org/https://doi.org/10.1002/qj.2060>, 2013.
- Holton, J. R.: *An Introduction to Dynamic Meteorology*, Academic Press, fourth edn., 553 pp., 2004.
- Hoskins, B. J., McIntyre, M. E., and Robertson, A. W.: On the use and significance of isentropic potential vorticity maps, *Quart. J. Roy. Meteor. Soc.*, 111, 877–946, <https://doi.org/10.1002/qj.49711147002>, 1985.
- Humpherys, J., Redd, P., and West, J.: A Fresh Look at the Kalman Filter, *SIAM Review*, 54, 801–823, <https://doi.org/10.1137/100799666>, 2012.
- Hunt, B. R., Kostelich, E. J., and Szunyogh, I.: Efficient data assimilation for spatiotemporal chaos: A local ensemble transform Kalman filter, *Physica D: Nonlinear Phenomena*, 230, 112–126, <https://doi.org/10.1016/j.physd.2006.11.008>, 2007.
- Isaksen, L., Hasler, J., Buizza, R., and Leutbecher, M.: The new Ensemble of Data Assimilations., ECMWF Newsletter 123, ECMWF, Shinfield Park, Reading, Berkshire, RG2 9AX, UK, available at <http://www.ecmwf.int/publications>, 2010.
- Janjić, T., Bormann, N., Bocquet, M., Carton, J. A., Cohn, S. E., Dance, S. L., Losa, S. N., Nichols, N. K., Potthast, R., Waller, J. A., and Weston, P.: On the representation error in data assimilation, *Quart. J. Roy. Meteor. Soc.*, 144, 1257–1278, <https://doi.org/https://doi.org/10.1002/qj.3130>, 2018.
- Joos, H. and Forbes, R. M.: Impact of different IFS microphysics on a warm conveyor belt and the downstream flow evolution, *Quart. J. Roy. Meteor. Soc.*, 142, 2727–2739, <https://doi.org/https://doi.org/10.1002/qj.2863>, 2016.
- Judt, F.: Insights into Atmospheric Predictability through Global Convection-Permitting Model Simulations, *J. Atmos. Sci.*, 75, 1477 – 1497, <https://doi.org/10.1175/JAS-D-17-0343.1>, 2018.
- Laloyaux, P., Bonavita, M., Chrust, M., and Gürol, S.: Exploring the potential and limitations of weak-constraint 4D-Var, *Quart. J. Roy. Meteor. Soc.*, 146, 4067–4082, <https://doi.org/10.1002/qj.3891>, 2020.

- 1045 Lang, S. T. K., Dawson, A., Diamantakis, M., Dueben, P., Hatfield, S., Leutbecher, M., Palmer, T., Prates, F., Roberts, C. D., Sandu, I., and Wedi, N.: More accuracy with less precision, *Quart. J. Roy. Meteor. Soc.*, n/a, <https://doi.org/https://doi.org/10.1002/qj.4181>, 2021.
- Leutbecher, M. and Lang, S. T. K.: On the reliability of ensemble variance in subspaces defined by singular vectors, *Quart. J. Roy. Meteor. Soc.*, 140, 1453–1466, <https://doi.org/10.1002/qj.2229>, 2014.
- Leutbecher, M. and Palmer, T. N.: Ensemble Forecasting, *J. Comp. Phys.*, 227, 3515–3539, <https://doi.org/10.1016/j.jcp.2007.02.014>, also
1050 available as ECMWF Tech. Memo. 514, 2008.
- Lewis, J. M.: Roots of Ensemble Forecasting, *Mon. Wea. Rev.*, 133, 1865–1885, <https://doi.org/10.1175/MWR2949.1>, 2005.
- Lillo, S. P. and Parsons, D. B.: Investigating the dynamics of error growth in ECMWF medium-range forecast busts, *Quart. J. Roy. Meteor. Soc.*, 143, 1211–1226, <https://doi.org/10.1002/qj.2938>, 2017.
- Lorenz, E. N.: Deterministic non periodic flow, *J. Atmos. Sci.*, 20, 130–141, [https://doi.org/10.1175/1520-0469\(1963\)020<0130:DNF>2.0.CO;2](https://doi.org/10.1175/1520-0469(1963)020<0130:DNF>2.0.CO;2), 1963.
- 1055 Lorenz, E. N.: Predictability; Does the flap of a Butterfly’s wings in Brazil Set Off a Tornado in Texas?, Presented at the American Association for the Advancement of Science, 139th meeting, https://web.archive.org/web/20130612164541/http://eaps4.mit.edu/research/Lorenz/Butterfly_1972.pdf, archived 2013-06-12 at the Wayback Machine, Accessed: 2021-11-11, 1972.
- Madonna, E., Wernli, H., Joos, H., and Martius, O.: Warm Conveyor Belts in the ERA-Interim Dataset (1979–2010). Part I: Climatology and
1060 Potential Vorticity Evolution, *J. Climate*, 27, 3–26, <https://doi.org/10.1175/JCLI-D-12-00720.1>, 2014.
- Magnusson, L., Nycander, J., and Källén, E.: Flow-dependent versus flow-independent initial perturbations for ensemble prediction, *Tellus A: Dynamic Meteorology and Oceanography*, 61, 194–209, <https://doi.org/10.1111/j.1600-0870.2008.00385.x>, 2009.
- McCabe, A., Swinbank, R., Tennant, W., and Lock, A.: Representing model uncertainty in the Met Office convection-permitting ensemble prediction system and its impact on fog forecasting, *Quart. J. Roy. Meteor. Soc.*, 142, 2897–2910, <https://doi.org/10.1002/qj.2876>, 2016.
- 1065 Molteni, F. and Palmer, T. N.: Predictability and finite-time instability of the northern winter circulation, *Quart. J. Roy. Meteor. Soc.*, 119, 269–298, <https://doi.org/10.1002/qj.49711951004>, 1993.
- Molteni, F., Buizza, R., Palmer, T. N., and Petroliagis, T.: The ECMWF Ensemble Prediction System: Methodology and validation, *Quart. J. Roy. Meteor. Soc.*, 122, 73–119, <https://doi.org/10.1002/qj.49712252905>, 1996.
- Oertel, A., Boettcher, M., Joos, H., Sprenger, M., and Wernli, H.: Potential vorticity structure of embedded convection in a warm conveyor
1070 belt and its relevance for large-scale dynamics, *Weather Clim. Dynam.*, 1, 127–153, <https://doi.org/10.5194/wcd-1-127-2020>, 2020.
- Palmer, T., Döering, A., and Seregin, G.: The real butterfly effect, *Nonlinearity*, 27, R123–R141, <https://doi.org/10.1088/0951-7715/27/9/r123>, 2014.
- Palmer, T. N., Molteni, F., Mureau, R., Buizza, R., Chapelet, P., and Tribbia, J.: Ensemble prediction, Tech. rep., ECMWF, Shinfield Park, Reading, Berkshire RG2 9AX, UK, available at <http://www.ecmwf.int/publications>, 1992.
- 1075 Portmann, R., González-Alemán, J. J., Sprenger, M., and Wernli, H.: How an uncertain short-wave perturbation on the North Atlantic wave guide affects the forecast of an intense Mediterranean cyclone (Medicane Zorbas), *Weather Clim. Dynam.*, 1, 597–615, <https://doi.org/10.5194/wcd-1-597-2020>, 2020.
- Rabier, F., Järvinen, H., Klinker, E., Mahfouf, J.-F., and Simmons, A.: The ECMWF operational implementation of four-dimensional variational assimilation. I: Experimental results with simplified physics, *Quart. J. Roy. Meteor. Soc.*, 126, 1143–1170, <https://doi.org/10.1002/qj.49712656415>, 2000.
- 1080 Rennie, M. P., Isaksen, L., Weiler, F., de Kloe, J., Kanitz, T., and Reitebuch, O.: The impact of Aeolus wind retrievals on ECMWF global weather forecasts, *Quart. J. Roy. Meteor. Soc.*, 147, 3555–3586, <https://doi.org/https://doi.org/10.1002/qj.4142>, 2021.

- Riemer, M. and Jones, S. C.: Interaction of a tropical cyclone with a high-amplitude, midlatitude wave pattern: Waviness analysis, trough deformation and track bifurcation, *Quart. J. Roy. Meteor. Soc.*, 140, 1362–1376, <https://doi.org/https://doi.org/10.1002/qj.2221>, 2014.
- 1085 Rodwell, M. J., Magnusson, L., Bauer, P., Bechtold, P., Bonavita, M., Cardinali, C., Diamantakis, M., Earnshaw, P., Garcia-Mendez, A., Isaksen, L., Källén, E., Klocke, D., Lopez, P., McNally, T., Persson, A., Prates, F., and Wedi, N.: Characteristics of occasional poor medium-range weather forecasts for Europe, *Bull. Amer. Meteor. Soc.*, 94, 1393–1405, <https://doi.org/10.1175/BAMS-D-12-00099.1>, 2013.
- Rodwell, M. J., Lang, S. T. K., Ingleby, N. B., Bormann, N., Hólm, E., Rabier, F., Richardson, D. S., and Yamaguchi, M.: Reliability in ensemble data assimilation, *Quart. J. Roy. Meteor. Soc.*, 142, 443–454, <https://doi.org/10.1002/qj.2663>, 2016.
- 1090 Rodwell, M. J., Richardson, D. S., Parsons, D. B., and Wernli, H.: Flow-Dependent Reliability: A Path to More Skillful Ensemble Forecasts, *Bull. Amer. Meteor. Soc.*, 99, 1015–1026, <https://doi.org/10.1175/BAMS-D-17-0027.1>, 2018.
- Rodwell, M. J., Hammond, J., Thornton, S., and Richardson, D. S.: User decisions, and how these could guide developments in probabilistic forecasting, *Quart. J. Roy. Meteor. Soc.*, 146, 3266–3284, <https://doi.org/10.1002/qj.3845>, 2020.
- 1095 Saetra, Ø., Hersbach, H., Bidlot, J. R., and Richardson, D. S.: Effects of Observation Errors on the Statistics for Ensemble Spread and Reliability, *Mon. Wea. Rev.*, 132, 1487–1501, [https://doi.org/10.1175/1520-0493\(2004\)132<1487:EOOEOT>2.0.CO;2](https://doi.org/10.1175/1520-0493(2004)132<1487:EOOEOT>2.0.CO;2), 2004.
- Sanders, F.: The evaluation of subjective probability forecasts, *Sci. Rept. 5*, MIT, Dept. of Earth, Atmospheric and Planetary Sciences, 77 Massachusetts Avenue, Cambridge, MA 02139-4307, USA, 63 pp., 1958.
- Sanders, F. and Hoskins, B. J.: An Easy Method for Estimation of Q-Vectors from Weather Maps, *Wea. Forecasting*, 5, 346 – 353, [https://doi.org/10.1175/1520-0434\(1990\)005<0346:AEMFEO>2.0.CO;2](https://doi.org/10.1175/1520-0434(1990)005<0346:AEMFEO>2.0.CO;2), 1990.
- 1100 Selz, T., Riemer, M., and Craig, G. C.: The Transition from Practical to Intrinsic Predictability of Midlatitude Weather, *Journal of the Atmospheric Sciences*, 79, 2013–2030, <https://doi.org/10.1175/JAS-D-21-0271.1>, 2022.
- Shutts, G. J.: A stochastic kinetic energy backscatter algorithm for use in ensemble prediction systems, *Tech. Rep. 449*, ECMWF, Shinfield Park, Reading, Berkshire RG2 9AX, UK, 2004.
- 1105 Sun, Y. Q. and Zhang, F.: Intrinsic versus Practical Limits of Atmospheric Predictability and the Significance of the Butterfly Effect, *J. Atmos. Sci.*, 73, 1419–1438, <https://doi.org/10.1175/JAS-D-15-0142.1>, 2016.
- Sutton, O. G.: The development of meteorology as an exact science, *Quart. J. Roy. Meteor. Soc.*, 80, 328–338, <https://doi.org/10.1002/qj.49708034503>, 1954.
- Swinbank, R., Kyouda, M., Buchanan, P., Froude, L., Hamill, T. M., Hewson, T. D., Keller, J. H., Matsueda, M., Methven, J., Pappenberger, F., Scheuerer, M., Titley, H. A., Wilson, L., and Yamaguchi, M.: The TIGGE Project and Its Achievements, *Bull. Amer. Meteor. Soc.*, 97, 49–67, <https://doi.org/10.1175/BAMS-D-13-00191.1>, 2016.
- 1110 Tiedtke, M.: A Comprehensive Mass Flux Scheme for Cumulus Parameterization in Large-Scale Models, *Mon. Wea. Rev.*, 117, 1779–1800, 1989.
- Tribbia, J. J. and Baumhefner, D. P.: Scale Interactions and Atmospheric Predictability: An Updated Perspective, *Mon. Wea. Rev.*, 132, 703–713, [https://doi.org/10.1175/1520-0493\(2004\)132<0703:SIAAPA>2.0.CO;2](https://doi.org/10.1175/1520-0493(2004)132<0703:SIAAPA>2.0.CO;2), 2004.
- 1115 Váña, F., Düben, P., Lang, S., Palmer, T., Leutbecher, M., Salmond, D., and Carver, G.: Single Precision in Weather Forecasting Models: An Evaluation with the IFS, *Mon. Wea. Rev.*, 145, 495–502, <https://doi.org/10.1175/MWR-D-16-0228.1>, 2017.
- Wedi, N. P., Polichtchouk, I., Dueben, P., Anantharaj, V. G., Bauer, P., Boussetta, S., Browne, P., Deconinck, W., Gaudin, W., Hadade, I., Hatfield, S., Iffrig, O., Lopez, P., Maciel, P., Mueller, A., Saarinen, S., Sandu, I., Quintino, T., and Vitart, F.: A Baseline for

- 1120 Global Weather and Climate Simulations at 1 km Resolution, *Journal of Advances in Modeling Earth Systems*, 12, e2020MS002192, <https://doi.org/10.1029/2020MS002192>, 2020.
- Wernli, H. and Davies, H. C.: A Lagrangian-based analysis of extratropical cyclones. I: The method and some applications, *Quart. J. Roy. Meteor. Soc.*, 123, 467–489, <https://doi.org/10.1002/qj.49712353811>, 1997.
- Wernli, H. and Schwerz, C.: Surface Cyclones in the ERA-40 Dataset (1958–2001). Part I: Novel Identification Method and Global Climatology, *J. Atmos. Sci.*, 63, 2486 – 2507, <https://doi.org/10.1175/JAS3766.1>, 2006.
- 1125